Imaging of magnetic structures by photoemission electron microscopy

Imaging of magnetic structures by photoemission electron microscopy

G Schönhense

Institut für Physik, Johannes Gutenberg Universität Mainz, Staudinger Weg 7, 55099 Mainz, Germany

Abstract. Photoemission electron microscopy (PEEM) has proven to be a powerful analytical tool in surface science. In this contribution, a status report is given on the application of the PEEM technique in the investigation of surface and interface magnetism. Owing to its fast parallel image acquisition and its wide zoom range, allowing fields of view from almost 1 mm down to a few micrometres, combined with a high base resolution of the order of 20 nm, the method offers a unique access to many aspects in surface and thin-film magnetism on the mesoscopic length scale. There are three basically different modes of magnetic imaging using PEEM. The first one exploits the magnetic x-ray circular dichroism (MXCD) for contrast formation. It offers the important advantage of selecting the magnetic contrast of a certain element via the corresponding x-ray absorption edges using a tuneable x-ray source such as synchrotron radiation. This mode gives access to magnetic structures and coupling phenomena with a sensitivity in the submonolayer range and the capability to image the signal of buried layers with an information depth up to more than 5 nm. The two other modes work with simple UV light sources and are therefore highly attractive for standard laboratory applications. The magnetic stray-field-induced changes of the electron trajectories close to the sample surface lead to a Lorentz-type contrast. A third type of contrast arises as a consequence of the Kerr rotation of the dielectric vector inside a magnetic material, a phenomenon which is also responsible for the well known magneto-optical Kerr effect. Examples and typical applications of magnetic imaging using PEEM are discussed.

1. Introduction

In a *photoemission electron microscope* (PEEM) the image formation is based on the lateral photoelectron intensity distribution from a solid sample surface. Experimentally there are two different approaches. The first utilizes a well focused photon beam which is scanned across the surface, the second employs parallel imaging techniques making use of special electron optics. This second approach is discussed in the present article. Early work goes back to the 1930s, when Brüche and Johannson [1–3] and Recknagel [4, 5] investigated the so-called cathode-lens microscopy experimentally and theoretically, respectively. Although the method has been continuously used and developed since these early years [6–18], the last two decades in particular had a strong impact on this field [19–36]. One important step was the introduction of ultrahigh vacuum technology in emission microscopy. Here the PEEM technique benefited a great deal from the development of the low-energy electron microscope (LEEM) by Bauer's group in Clausthal [22–25]. Another important benefit came along with the availability of synchrotron radiation sources with steadily-increasing performance. High brilliance combined with easy tuneability and polarizability make synchrotron radiation the ideal excitation source for a PEEM.

Today, there are several main areas of application of PEEM: one is the investigation of chemical surface reactions, e.g. the real time observation of the spacio-temporal behaviour of catalytic reactions by Ertl *et al* [37], another one is the element specific imaging of surfaces using tuneable x-rays from a synchrotron radiation source, demonstrated 1988 for the first time by Tonner and Harp [38]. A third area is magnetic domain imaging exploiting magnetic x-ray circular dichroism (MXCD), discussed in section 3. The pioneering experiments using MXCD for contrast formation have been performed 1993 by Stöhr *et al* [39]. These experiments have initiated a great increase in activity in several groups, making use of the circularly-polarized synchrotron radiation from storage rings all over the world.

The interest in *magnetic domain imaging in the sub-micrometre range* has been rapidly increasing during the last decade. A considerable impetus is coming from the development of high-density magnetic storage devices and from the forthcoming achievements of spin electronics. In order to tailor the magnetic behaviour of these systems to specified needs, for instance, a certain response to magnetization reversal, a detailed understanding of the structure and dynamics of magnetic domains is mandatory. In addition, the thin film nature of such devices emphasizes the surface aspect of magnetism. This situation asks for magnetic domain imaging techniques which combine surface sensitivity with high lateral resolution. These requirements pose a considerable challenge to conventional domain imaging techniques. In magneto-optical Kerr microscopy [40–42], for example, the resolution is limited by the photon wavelength. Lorentz microscopy [43–45], being based on the transmission of a high-energy electron beam, lacks surface sensitivity. To overcome these principal limitations, various high-resolution approaches involving alternative physical principles of magnetic contrast formation have been developed, such as scanning electron microscopy with polarization analysis (SEMPA) [46–48], magnetic force microscopy (MFM) [49–52], scanning transmission x-ray microscopy [53–55], imaging transmission x-ray microscopy (TXM) [56], scanning near-field optical microscopy (SNOM) [57, 58], spin-polarized scanning tunnelling microscopy (SP-STM) [59], a spin-polarized version of low-energy electron microscopy (SP-LEEM) [60–63] or the various PEEM techniques discussed in the following sections. Compared to the parallel imaging techniques, i.e. Kerr- and Lorentz-microscopy, TXM, LEEM and PEEM, the sequential (scanning) approach is generally slower, thus impairing real-time studies.

For many applications *element specificity* is even more important than high lateral resolution. Materials of magnetic storage media or the building elements of spin-electronic devices are often composed of several chemical elements or intermetallic compounds, each of which distinctly contributes to the magnetic behaviour. It thus becomes necessary to distinguish the various magnetically active components in a system. An 'ideal' magnetic imaging technique should combine magnetic sensitivity with element specificity, in a resolution range well below the size of the magnetic structures.

In a PEEM, element-specific magnetic imaging exploiting MXCD at a selected x-ray absorption edge provides easy *access to buried layers*. Stöhr *et al* [64] have found that the MXCD signal can still be detected through a 10 nm thick layer of Rh or Ag. Siegmann *et al* [65, 66] have shown that the escape depth in transition metals is largely determined by scattering processes from filled to empty states and is therefore inversely proportional to the number of d-holes. According to this rule, the magnetic probing depth strongly depends on the material of the top layer. It is highest for materials with completely filled d bands like Cu, Ag or Au. For non-metallic top layers there is not much information available at present. Ade *et al* [67] have successfully detected Ti dots buried under as much as 40 nm of AlN grown by chemical vapour deposition in PEEM with ultraviolet excitation at $h\nu = 5$–6 eV. Since AlN has a large band gap of $\sim$6.2 eV and a negative electron affinity, however, this may represent a special case.

In this paper a status report on the magnetic imaging techniques using PEEM is given. After a description of the principle of operation in section 2, the three different modes of magnetic imaging in a PEEM will be described in sections 3–5 along with various typical applications.

2. The technique of photoemission electron microscopy

Unlike all common types of electron microscope the PEEM is based on a 'hybrid technique': it combines optical excitation with electron-optical imaging. The main advantages of the PEEM technique are its fast parallel image acquisition, similar to that of an optical microscope, and the high lateral resolution of typically 10–20 nm, depending on the sample and illumination source. The electron optical lens system allows us to 'zoom' the field of view from almost 1 mm down to a few micrometres in size, which is ideal for the investigation of magnetic structures. Rempfer *et al* [19, 20] reported an ultimate resolution of about 8–10 nm. In the future, the integration of correctors (special elements for the correction of the spherical and chromatic aberrations) should drive the resolution limit down to the range of 1 nm as calculated by Rose *et al* [68]. However, topographical features as well as electric and magnetic stray fields close to the sample surface (e.g. due to workfunction differences or magnetic structures) significantly change the electron trajectories. This sets a practical limit to the ultimate lateral resolution [69].

If a photon energy just above the photothreshold is used, the photoelectron yield is mainly determined by differences in the work function Φ of the sample. The local variations of Φ result in images with a high contrast. This *UV-PEEM* mode of operation (threshold photoemission) is ideally suited to study surface chemical reactions in real time [37]. The resulting image contrast in UV-PEEM is mainly due to work function differences or variation of crystallinity, topography, adsorbate coverage or chemical composition across the surface.

With the advent of high-brilliance synchrotron radiation from storage rings, the new and highly attractive *X-PEEM* mode of operation became possible. By tuning the photon energy to a characteristic x-ray absorption edge, the lateral emission distribution of the selected element becomes visible. If, in addition, circularly polarized radiation is used, the magnetic x-ray circular dichroism (MXCD) can be exploited to generate a magnetic contrast [39].

The heart of each emission microscope is the cathode lens, because its aberrations determine the limit of the lateral resolution and the possible range of the field of view. Depending on the number of electrodes we distinguish between triode and tetrode lenses. Chmelik *et al* [70] give a quantitative comparison of the various types of cathode lens. For the study of magnetic samples any magnetic stray fields close to the sample must be avoided. Therefore, a purely electrostatic lens system is advantageous. Figure 1 illustrates the operation of such an electrostatic cathode lens. This design combines the high-resolution properties of a tetrode with the advantage of a triode, i.e. the distortion-free imaging of a very large field of view of almost 1 mm. In the high-resolution mode of operation (left part of the figure) the extractor electrode is kept at a high positive voltage (U_{extr} typically 15 kV). This results in a field strength of about 7 kV mm^{-1}, which leads to an efficient extraction of the low-energy electrons from the sample (being at ground potential). In this mode, the electric field strength is the main limiting factor for the ultimate resolution. In the triode-like mode of operation (right part) the extractor electrode is kept on an equipotential contour of the field distribution between sample and focus electrode. In this mode the electric field strength at the sample surface is only small (of the order of 100 V mm^{-1}), but a large field of view is accepted by the lens. In this 'survey mode' the lateral resolution is limited to about 1 μm. In such a cathode lens the sample is an integral part of the lens and must be flat and well aligned perpendicular to the optical axis.
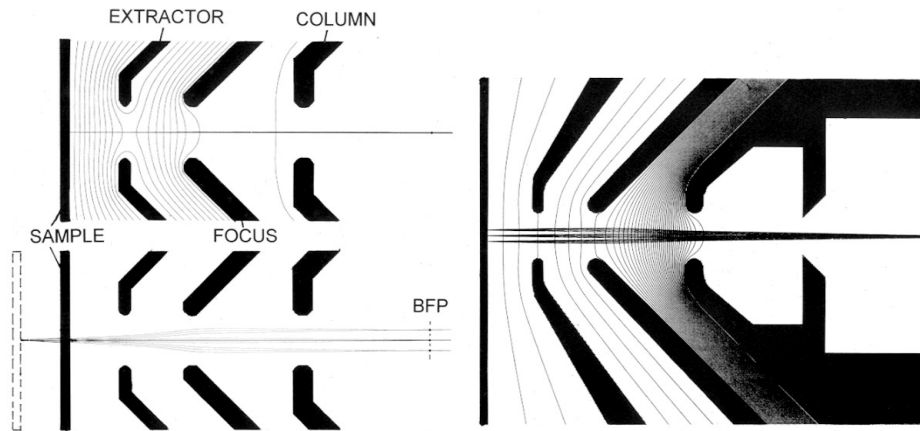
Figure 1. Electrostatic cathode lens with equipotential contours and photoelectron trajectories. The lens can be either operated in the high-resolution tetrode mode (left) or in the triode-like 'survey mode' (right), characterized by a large field of view. (Trajectory parameters: top left, $E_0 = 0.1$ eV; $\alpha_0 = 0$–$90°$; bottom left, $E_0 = 100$ eV, $\alpha_0 = 0°$, $\pm 20°$; right, $E_0 = 0.1$ eV, $\alpha = -30$–$+30°$, field of view, 0.5 mm diameter.) (Simulation courtesy M Escher, FOCUS GmbH.)

The trajectories in the lower left part of figure 1 illustrate that the asymmetric einzel-lens (immersion lens) defined by the extractor/focus/column electrodes 'sees' a virtual image of the sample (dashed) with an apparently much higher electron starting energy E' given by

$$E' = E_0 + eU_{extr} \tag{1}$$

and a much smaller starting angle α' given by

$$\alpha' = \alpha_0 (E_0/E')^{1/2}. \tag{2}$$

E_0 and α_0 are the true starting energy and starting angle with respect to the surface normal; $eU_{extr} \approx 15$ keV is the energy gain in the tetrode mode for the electrons when reaching the extractor electrode. The distance of the virtual sample image from the extractor electrode is about twice as large as the true distance. These results as well as the capability of high resolution in the 10 nm range have been analytically derived by Recknagel [4, 5] and Brüche [3]. They have shown that the lateral resolution δ_{acc} in the virtual image (magnification 1) of the sample produced by the acceleration field is approximately given by the simple relation

$$\delta_{acc} \approx \sqrt{2} \frac{E_0}{eF}. \tag{3}$$

Here F is the electric field strength at the sample surface. This relation holds for small starting energies E_0 and energy widths $\Delta E \approx E_0$ if no contrast aperture is used, i.e. all starting angles are accepted by the lens system. For typical conditions in threshold PEEM the resolution is limited to values above $\delta_{acc} \approx 0.1$ μm unless the beam is restricted by a contrast aperture.

The expressions for the chromatic aberration δ_c and spherical aberration δ_s of the objective lens are determined by the 'apparent quantities' of the virtual sample image as defined in equations (1) and (2).

$$\delta_c = C_c \alpha' \frac{\Delta E}{E'} \tag{4}$$

$$\delta_s = C_s \alpha'^3. \tag{5}$$

In the UV-PEEM mode the chromatic aberration is relatively small, because the energy width of typically $\Delta E \approx 0.1$–0.5 eV is referred to the *high energy E'* and the spherical aberration

is analogously defined by the *small angle* α'. The coefficients C_c and C_s characterize the aberrations of the lens itself. Owing to this transformation to the high-energy phase space caused by the acceleration field, the aberrations of a properly designed lens can be kept smaller than the aberration of the acceleration field, if a suitable contrast aperture is used to reduce the angle α'. In the X-PEEM mode the energy width ΔE of the secondary electrons forming the image is larger, typically several electronvolts. In this case the chromatic aberration of the acceleration field and lens becomes the dominant contribution. For small diameters of the contrast aperture the diffraction contribution δ_d must be taken into account

$$\delta_d = \frac{0.61\lambda}{\alpha'} \tag{6}$$

with λ being the wavelength of the electron after acceleration to the column potential. The final aberration disc is defined by the square root of the sum of the squares of all terms

$$\delta_{tot} = \sqrt{\delta_c^2 + \delta_s^2 + \delta_d^2} \tag{7}$$

a relation which is only approximately valid [71].

Owing to the acceleration field the cathode lens exhibits a pronounced low-pass transmission characteristic as can be seen in the two cases for $E_0 = 0.1$ eV (top) and $E_0 = 100$ eV (bottom) on the left-hand side of figure 1.

Figure 2 shows the electron-optical layout of a typical instrument (Focus IS-PEEM). The sample being illuminated by the UV or x-ray beam is located in front of the electrostatic immersion objective lens as described in figure 1. The final magnification is obtained by two projective lenses followed by an image intensifier (multichannel plate) and a fluorescent screen. The visible image can be viewed by a CCD camera, e.g. a cooled slow-scan camera with typically 1024×1024 pixels. Image contrast and intensity can be optimized by means of a piezomotor-driven selectable and adjustable contrast aperture in the backfocal plane of the objective lens. This aperture defines the angle α', i.e. the size of the chromatic and spherical aberrations according to equations (4) and (5), as well as the diffraction term which becomes significant for very small angles α' according to equation (6). An octopole stigmator/deflector allows correction of the astigmatism as well as a lateral adjustment of the field of view on the sample surface. A continuously variable field aperture (iris) in the first intermediate image plane allows the definition of the field of view, in particular for microspectroscopy purposes. The three-lens combination facilitates selection of regions between 0.7 mm and a few micrometres field of view. In order to eliminate a deterioration of resolution due to vibrations, a piezomotor-driven x/y sample stage is integrated into the microscope head.

The bottom left panel of figure 1 illustrates the action of the contrast aperture in the backfocal plane (BFP) of the objective lens. Here, the lens produces a reciprocal image, i.e. a diffraction pattern. Consequently, there is a direct relationship between the diameter of the contrast aperture and the cone of electron starting angles on the sample surface being accepted by the microscope optics at a given starting energy. The trajectories of the lower left figure indicate that the strong acceleration field in front of the sample surface leads to an effective collection of the electrons (here $E_0 = 100$ eV). In the backfocal plane the different starting angles appear spatially resolved, as in a diffraction pattern (LEED pattern).

The advantage of the hybrid technique of photon excitation and electron imaging is that all analytical techniques based on x-ray excitation can be easily incorporated and thus combined with high spatial resolution. This has been demonstrated for x-ray absorption spectroscopy (XAS) or the x-ray absorption near edge structure (XANES) [72–74] as well as extended x-ray absorption fine structure (EXAFS) [74]. If an additional electron energy analyser is integrated into the microscope column, also imaging or small-spot ESCA (electron spectroscopy for chemical analysis) is possible using the PEEM method [68, 75–78].
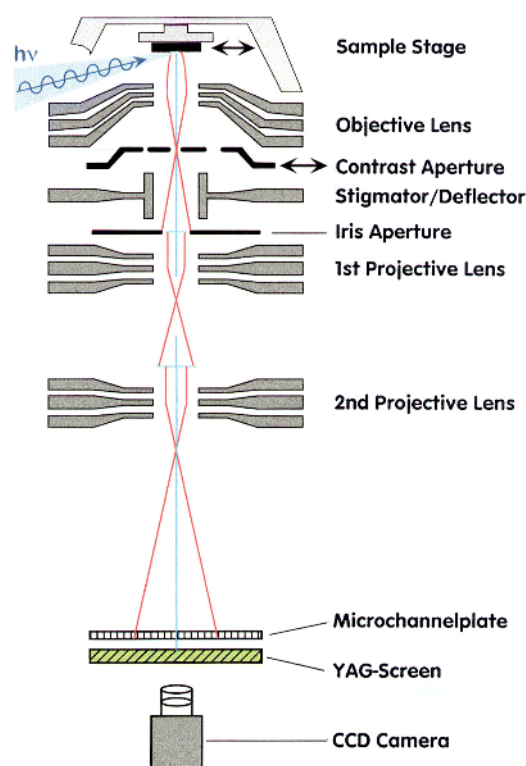
Figure 2. Schematic set-up of a photoemission electron microscope (Focus IS-PEEM) with an integral sample stage, variable contrast aperture, octopole stigmator/deflector and continuously variable field aperture. The electron optics is a three-lens system.

Employing time-resolved electron detection in a PEEM, dynamic processes were observed by Bostanjoglo *et al* [79]. More recently, the novel application of time-of-flight-(TOF-)PEEM has been established by Spiecker *et al* [80] using an ultrafast CCD camera and by Oelsner *et al* [81] using a space- and time-resolving delayline detector as electron counting device. Present time resolution is about 400 ps with the potential for further improvement. This novel technique is highly attractive for use in the future for real-time observation of dynamic magnetization processes.

For the MXCD experiments discussed in section 3, circularly-polarized radiation in the soft x-ray range is required. At present, the only source which delivers a sufficiently high brightness for X-PEEM is synchrotron radiation. At a bending-magnet beamline the circular polarization can be achieved by selecting that part of the photon beam which is emitted above or below the storage ring plane, like the PM3 monochromator of BESSY I in Berlin. A much higher brilliance is obtained at insertion devices like wigglers and undulators which are especially designed for the production of circularly-polarized radiation, like the ID12B of the ESRF in Grenoble. These beamlines were used for the experiments discussed in section 3, and details can be found in [82]. The UV-PEEM techniques discussed in sections 4 and 5 require only UV light from simple laboratory lamps. This is an important advantage for standard applications.

In this context, it is worth mentioning that there has been a rapid development of laboratory-based soft x-ray sources, in particular for the demands of XUV lithography. Incoherent sources, like the laser-induced plasma, deliver characteristic lines or quasi-continua of the selected target

material [83]. More recently, coherent soft x-ray radiation has been produced via frequency conversion in a gas cell [84]. Such sources deliver many-line spectra and can cover a photon energy range up to several 100 eV using an x-ray monochromator. In addition, the efficiency of x-ray optical elements like multilayer-coated mirrors, zone plates or tapered capillary optics has been considerably improved. It is therefore not unlikely that laboratory-based x-ray sources suitable for X-PEEM will become available on a time scale of several years from now. Recently, Ade *et al* [67] reported the first experiment employing a free electron laser (in the UV range) as the excitation source of ultimate brightness for PEEM.

3. Element-selective domain imaging utilizing magnetic x-ray circular dichroism

3.1. Chemical and magnetic microspectroscopy

Chemical microspectroscopy in a standard PEEM (without energy filter) is based on x-ray absorption. The characteristic near-edge features of XANES show up in the electron emission yield as well. Hence, the intensity of a selected microarea in an image directly reflects the x-ray absorption spectrum if the photon energy is scanned.

Figure 3 shows an example of such a chemical spot analysis performed by Swiech *et al* [73]. A microstructured Permalloy film (squares of 20 μm $\times$ 20 μm) on a silicon wafer has been investigated using local XAS. In this mode of operation areas of interest are defined in the image (right part of the figure). Area selection is facilitated either electronically by setting regions in the software of the CCD camera or mechanically by closing the variable iris aperture of the PEEM to the desired size after centring the area of interest. Then, the energy of the exciting radiation is swept in the region of the relevant absorption edges. The electron intensity corresponding to the defined microspot is plotted versus the photon energy (left panel). In this case, the XAS microanalysis of a Permalloy square reflects the element distribution of $Fe_{19}Ni_{81}$ with its characteristic $L_{2,3}$ white lines (lower curve), whereas the analysis of the Permalloy-free bars reflects the photoyield of Si which is unstructured in this area (upper curve). Close inspection of the region of the Ni $L_{2,3}$ edges reveals traces of Ni diffusion onto the Si. Given the present conditions at BESSY I (monochromator PM 3 at a bending-magnet beamline), spot sizes of down to 500×500 nm^2 were possible. At synchrotron-radiation sources of the third generation such as BESSY II substantial improvements of microspot resolution will be possible due to the much higher brilliance (two to three orders of magnitude) characteristic of undulator beam lines.

For magnetic microspectroscopy the magnetic x-ray circular dichroism (MXCD) in the total photoyield at the $L_{2,3}$ absorption edges is exploited. The dichroic signal arises from the fact that the x-ray absorption cross section at the inner-shell absorption edges of aligned magnetic atoms depends on the relative orientation of the photon spin (helicity) and the local magnetization direction. The MXCD is quantified either in terms of the *absolute dichroic signal* ΔI_{MXCD} given by

$$\Delta I_{MXCD} = I_{RCP} - I_{LCP} \tag{8}$$

with I_{RCP} (I_{LCP}) denoting the intensity spectra taken for right (left) circularly-polarized radiation. Alternatively, one can plot the *MXCD asymmetry* A_{MXCD} which is a relative quantity which varies between -100% and $+100\%$

$$A_{MXCD} = \frac{I_{RCP} - I_{LCP}}{I_{RCP} + I_{LCP}}. \tag{9}$$

Figure 4 shows an example [73] taken at a small spot on one of the Permalloy squares of figure 3. Depending on photon helicity, the spin–orbit-split Fe $L_{2,3}$ edges appear at a different intensity (full and dotted curve, respectively). The sign of the dichroic signal is reversed at the
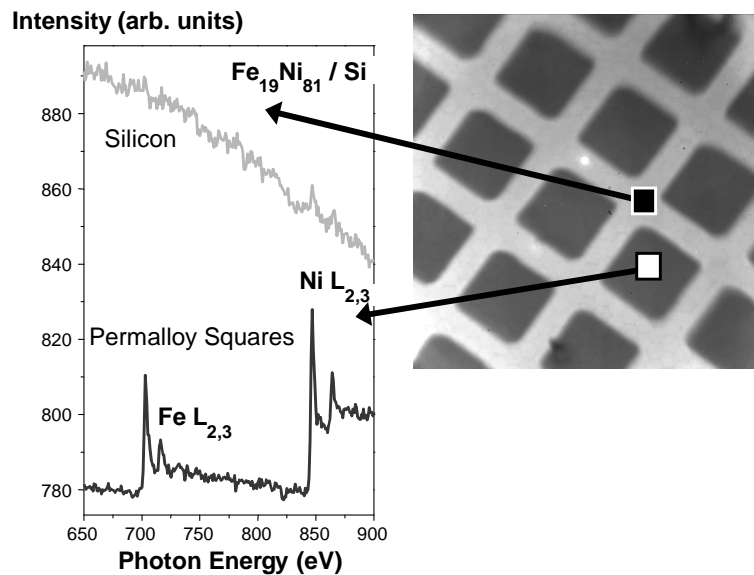
Figure 3. Chemical microspectroscopy of a Permalloy square array on silicon. Local element detection reveals a small amount of Ni on the Permalloy-free Si bars (from [73]).

two spin–orbit-split lines of 3d transition metals. This is characteristic for the behaviour of the optically-induced spin polarization in spin–orbit split states. For an initial p-state the size of the MXCD asymmetry should ideally exhibit the ratio 1:2 for the $p_{3/2}$ and $p_{1/2}$ sublevels, respectively. Relativistic effects may alter this branching ratio qualitatively.

Figure 4 suggests that high-contrast and laterally resolved magnetic domain patterns can be obtained either by subtracting images acquired at the L_2 and L_3 lines from each other or by subtracting images taken at the same line with different photon helicities. This utilization of MXCD as a kind of 'internal spin filter' (see below) substitutes time consuming electron spin-polarization analysis for direct imaging of magnetic domains.

3.2. Origin of the element-selective magnetic contrast

A decade ago it was shown by Schütz *et al* [85] by the example of the Fe K edges that absorption of circularly polarized x-rays depends on the magnetization state of the sample. For a fixed photon helicity (left or right circularly polarized) a characteristic change of the absorption spectra was observed when the magnetization vector M was switched from parallel to antiparallel orientation with respect to the direction of photon incidence q, or, more precisely, photon spin s_γ. This MXCD can be considered as the high-energy analogue of the magneto-optical Kerr effect. Both are based on the simultaneous action of spin–orbit coupling and exchange interaction in the electronic states being involved in the optical excitation. The fact that MXCD arises at the x-ray absorption edges provides an outstanding advantage for the element-selective investigation of magnetic phenomena.

The MXCD signal occurs in the x-ray absorption and electron yield signal, the latter containing more surface-specific information on magnetism. This effect is well suited for a combination with the PEEM technique for imaging of magnetic domains. The MXCD in the initial absorption signal is transferred to the emitted electrons in a two-step process (see figure 5,
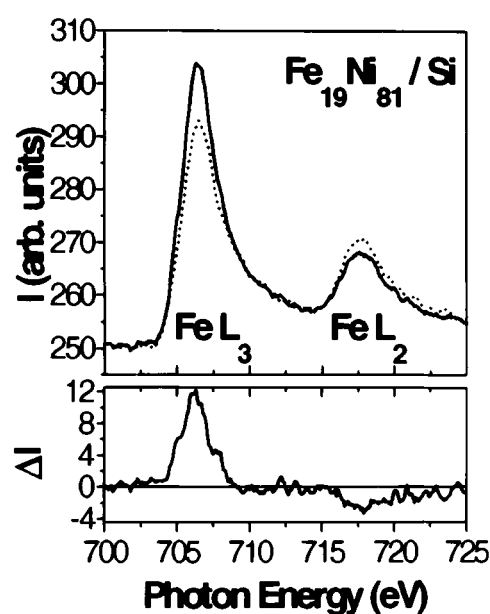
Figure 4. Magnetic microspectroscopy using magnetic x-ray circular dichroism (MXCD). Note that the sign of the dichroic signal ΔI is reversed at the spin–orbit-split $L_{2,3}$ shells of 3d transition metals (from [73]).

after [86, 87]). First, the optical excitation creates a core hole, in our example in the $2p_{3/2}$ shell. Owing to optical spin orientation by circularly-polarized light the excited electrons are spin polarized [88, 89]. Just above the absorption edge, the final state of the initial photoexcitation lies in the region of the unoccupied d band above the Fermi energy E_F. Since there is a high unoccupied density of states in the minority spin channel (right density of states in figure 5), primary electrons with this spin orientation are favoured, whereas the majority spin direction finds only a small part of the unoccupied band structure. This is the origin of the MXCD asymmetry in the initial photoabsorption step. The resulting different absorption cross section for opposite magnetization directions is equivalent to a different probability of the creation of a core hole. The spin quantization axis for the density of states is defined by $-M$, the optical spin orientation is aligned along the photon spin s_γ. Consequently the projection of s_γ onto M is a measure of the observed MXCD signal.

In a secondary step, the core hole decays with a final lifetime either through fluorescence or via an Auger process. In the latter case the magnetic dichroism in the absorption channel is directly transferred to the Auger electron yield. For parallel and antiparallel configuration of M and s_γ one thus obtains different intensities of the Auger transitions. This magnetic circular dichroism in the photon-induced Auger electron emission can be utilized for energy-selective imaging of magnetic domains in imaging ESCA as shown by Schneider *et al* [90]. Since in an Auger transition various angular momenta are involved, there could be quantitative changes of the MXCD signal when being transferred to the Auger channel [91].

On their way to the sample surface the characteristic Auger electrons experience inelastic scattering events and thus produce a cascade of secondary electrons. In a good approximation, the intensity of the secondary electrons is proportional to the number of initially excited Auger electrons. In this way, the MXCD signal created in the initial step of the photoexcitation is transferred via the intermediate step of the Auger electron emission finally to the low-energy
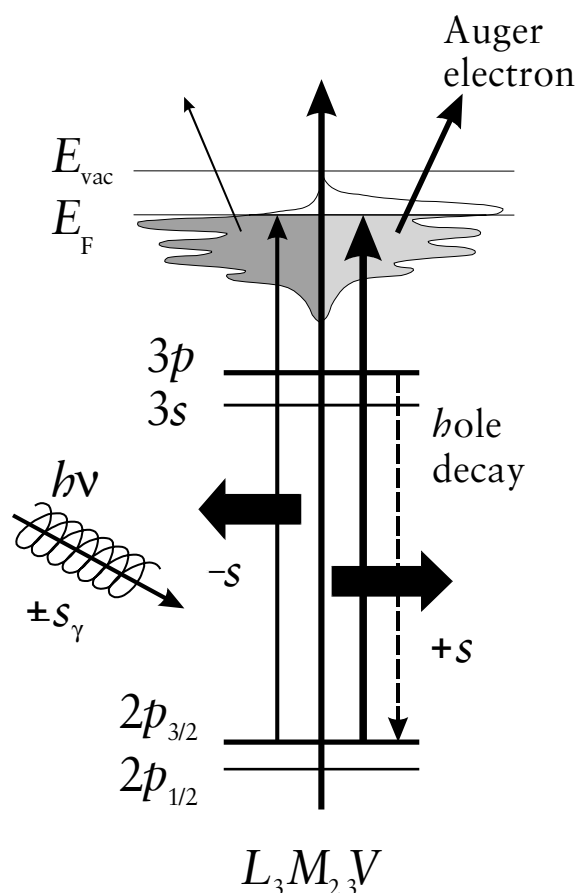
Figure 5. Origin of the magnetic circular dichroism in the electron yield. The dichroism asymmetry arises in the initial photoexcitation step from the core level into the spin-dependent unoccupied density of states just above E_F. The optical spin orientation due to the circularly polarized light leads to spin polarization of the photoexcited electrons. In turn, different transition probabilities into the majority and minority part of the band structure arise (different thickness of arrows). The core hole is filled via an Auger decay. Finally, the low energy secondary electrons are utilised for imaging.

secondary electrons. Except for the persisting MXCD asymmetry, these electrons carry no direct information about the specific electronic transition in the sample. However, element selectivity is ensured by the initial excitation at a characteristic absorption edge.

Since the cathode lens acts as an efficient low-pass filter, these secondary electrons in the region between threshold and a few electronvolts (depending on the size of the contrast aperture) are used for forming the image in the PEEM. The effective energy distribution is given by the secondary-electron spectrum convoluted with the transmission function of the microscope optics [92]. It peaks at an energy below 0.5 eV. This low energy of the image-forming electrons explains the surprisingly high probing depth as observed for materials with filled d-shells and for insulators (see the end of section 1). Actually the interplay between the x-ray absorption cross sections of both the cover material (defining the penetration depth) and the buried structure (defining the signal strength) as well as the Auger yield and mean free path of the low-energy secondaries defines the effective probing depth.

3.3. Imaging of magnetic structures and domain walls

The exploitation of the MXCD signal in the secondary electron yield as contrast mechanism allows a direct imaging of the domain structure of a selected element in a ferromagnetic sample. The parallel image acquisition in a PEEM and the combination of high magnetic contrast and high intensity of the secondary electrons facilitates very short exposure times. The method allows an aberration-free imaging of magnetic microstructures. Unlike the case in magnetic force microscopy the domain structure is not influenced by the PEEM method. The electrostatic objective lens in combination with an effective mu-metal shielding ensures the sample region being free of magnetic stray fields.

Figure 6 shows domain structures of regularly patterned microstructures of Permalloy (a), a Co/Pt multilayer (b) and a Co film (c) (from [73, 86 and 93], respectively). The first two samples were evaporated on an Si surface covered by native oxide, whereas the third one was epitaxially grown on a Cu(100) single crystal surface. The size of the squares was $20 \times 20 \ \mu m^2$ in (a) and (b) and $8 \times 8 \ \mu m^2$ in (c). The squares in (a) and (b) are separated by bars of uncovered silicon with a width of $7 \ \mu m$. All measurements were made at room temperature.
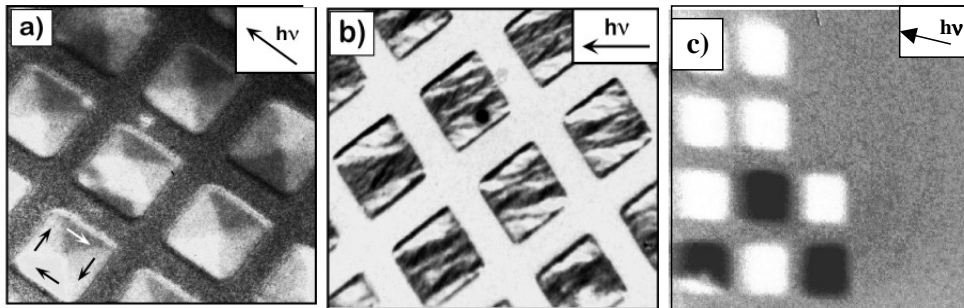

Figure 6. Magnetic domain structure in square arrays of thin films of Permalloy (a), a Co/Pt multilayer (b) and Co on Cu(100) (c). Different behaviour of the magnetic anisotropy causes different patterns of the magnetization (from [73, 86, 93], respectively).

In the case of the *Permalloy structure* (a) the domain pattern is made visible 'in the light of' the Fe $L_{2,3}$ edges. The image represents the difference of two images taken at the Fe L_3 and L_2 edges. Since the MXCD signal changes its sign when switching from the L_3 to the L_2 edge (cf figure 4), the magnetic information is thus effectively enhanced by suppressing nonmagnetic contrast contributions. Most Permalloy squares exhibit a very regular domain structure: four triangles, two of which appear in an intermediate grey level, while the two others appear darker and brighter. This distribution of the contrast can be understood by the angle dependence of the MXCD signal. For reasons of symmetry the magnetic contrast vanishes for an orthogonal arrangement of M and s_γ. The intermediate grey level indicates such domains with $M \perp s_\gamma$, whereas for the bright and dark domains M is parallel or antiparallel with respect to s_γ (except for the small tilt of $25°$ of the photon beam versus the surface plane). This consideration allows us to reconstruct the magnetization distribution within the squares. It has the shape of a typical flux-closure structure, i.e. each square tends to minimize its outer magnetic stray field. This configuration represents the simplest case of a flux-closure domain pattern and is obviously favoured by the vanishing magneto-crystalline anisotropy of Permalloy. However, this ideal case can be perturbed by defects on the surface, as visible for the square in the centre of the image. An interesting aspect for future experiments is a possible magnetic coupling between the squares and its influence on the domain pattern.

A material with a strong magneto-crystalline anisotropy, like the *Co/Pt multilayer*, shows a completely different behaviour (figure 6(b)). In this case the magnetic information has been obtained at the Co L_3 edge by changing the photon helicity [86]. Again, the magnetic signal is reversed and in the difference image only the magnetic contrast appears because all other contributions are cancelled. The resulting domain structure is much more complex than in the preceding case and varies in detail between the different squares. The feather-like features indicate locally varying easy directions of magnetization. This result is consistent with the polycrystalline character of the Co/Pt layers. This result represents a first example for the investigation of 'buried' layers. The topmost layer of the Co/Pt stack consists of approximately 3 nm Pt. Nonetheless, the element selectivity and information depth of the method allows us to investigate the magnetic signal of the Co layers through the Pt top layer.

The third example (figure 6(c)) shows another completely different behaviour [93]. In this case an *epitaxial Co film* of 15 monolayers thickness grown on a clean Cu(100) substrate has been investigated†. The domain structure of the film was observed at the Co L_3 edge in the 'as-grown' magnetic state. The [100] direction of the substrate was oriented parallel to the plane of incidence (indicated by the arrow). This leads to four equivalent easy axes of the in-plane magnetization of the Co film. A spontaneous magnetization of the Co squares along the four ⟨110⟩ directions would thus result in equal projections of either two of these easy axes along the direction of photon incidence. This would lead to the observation of only two different asymmetries in the present geometry. The experimental result of only two grey levels is thus compatible with the Co structures being magnetized along one of these fourfold crystallographic axes. Another explanation, i.e. the presence of a uniaxial in-plane anisotropy aligning the magnetization along one principal axis, cannot be excluded. Such a uniaxial anisotropy could be induced, for example, by atomic steps in the substrate due to a miscut [94, 95]. With a few exceptions only (e.g. the bottom left square), the Co squares appear in single-domain states with two different projections of the local magnetization vector onto the photon spin (dark and bright squares).

The angular dependence of MXCD explained above can also be exploited to selectively image *domain walls*. This experiment is based on the following consideration. In a domain wall the direction of the magnetization vector M varies continuously across the interface of two domains. In a Bloch wall occurring in the bulk, M rotates about an axis perpendicular to the plane of the wall thereby forming a spiral. At a surface, however, such a wall generates a magnetization component perpendicular to the surface. This state is energetically unfavourable and is avoided in soft magnetic material by the formation of a Néel-like wall. In this case M rotates about an axis perpendicular to the surface, i.e. M remains in the plane of the surface. This Néel termination of Bloch walls at the surface is well known from SEMPA [96]. In the region of the Néel wall a magnetization component occurs which lies in the surface and is oriented perpendicular to the domain magnetization direction. In a system of fourfold symmetry such as Fe(100) it has the consequence that for the geometries of $M \parallel s_\gamma$ or $M \perp s_\gamma$ one can selectively image either the domains or the domain walls, respectively.

An image of the domains and domain walls in the surface of an Fe(100) single crystal (whisker) is shown in figure 7 (from [86] and [97]). In 7(a) the strong 'black-and-white' contrast of the domains is visible; in 7(b) the $M \perp s_\gamma$ orientation is shown. In the major part of image 7(b) no magnetic domain contrast is visible because M is orthogonal to the plane of photon incidence. However, two pronounced zig-zag lines are observed. The contrast of each line changes from bright to dark in the positions indicated by the circles. The magnetization directions of the domains are indicated by the black arrows.

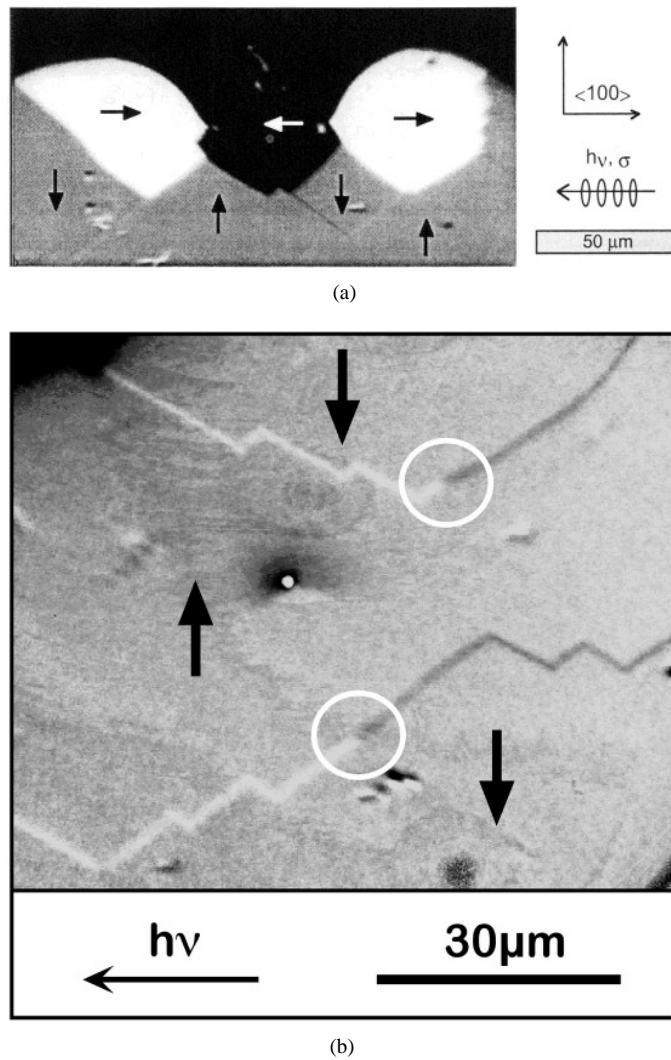† Actually, this layer was finally covered by Ni (cf section 3.4).

(a)

(b)

Figure 7. Domain structure (a) and domain walls (b) in the surface of an Fe(100) single crystal. Arrows denote the local orientations of the magnetization; circles mark the change in the sense of rotation of the magnetization in a domain wall, which leads to a contrast reversal (from [97] and [86], (a) and (b), respectively).

In principle, this magnetization distribution is energetically unfavourable and becomes stabilized by the bulk. It occurs when the magnetization deep in the bulk is oriented perpendicular to the surface. In order to reduce the magnetostatic energy, flux-closure domains are formed in the surface region, whose magnetization vectors lie in the surface plane. Consequently, domain walls in figure 7 are not simple 180° walls but rather so-called 'V-lines', indicative of 90° walls coming from the bulk and meeting at the surface [98]. Their width is approximately 500 nm. The resulting angle at the kinks of the curve in the image is 106°, which agrees very well with the value known for V-lines in Fe(100). A change of contrast observed along the line results from the fact that for Néel-like terminations of the domain walls at the surface two different senses of rotation of the magnetization are possible.

Hence, the rotation sense along the wall can flip from clockwise to anticlockwise (see circles). In the future, the detailed investigation of such structures and discontinuities will be one of the major challenges of magnetic photoelectron emission microscopy.

3.4. Investigation of exchange-coupled systems.

The potential to view 'buried' layers through top layers of different constituents using the element-resolved imaging technique is one of the striking advantages of magnetic X-PEEM. Except for the trivial case of a non-magnetic top layer none of the other imaging techniques mentioned in the introduction is capable of revealing the magnetic structure of a buried layer. TXM could work in principle if the layered structure is sufficiently thin and the x-ray optics allows tuneability over a photon energy range comprising the relevant absorption edges. In the following we will present a few examples in order to illustrate the performance of the X-PEEM technique.

Figure 8 shows the sandwich structure of a *Co film separated from an Fe substrate by a Cr wedge* for two different methods of preparation, i.e. deposition at slightly elevated temperature and at 500 K (from [86] and [93], respectively). The sample was prepared in the following
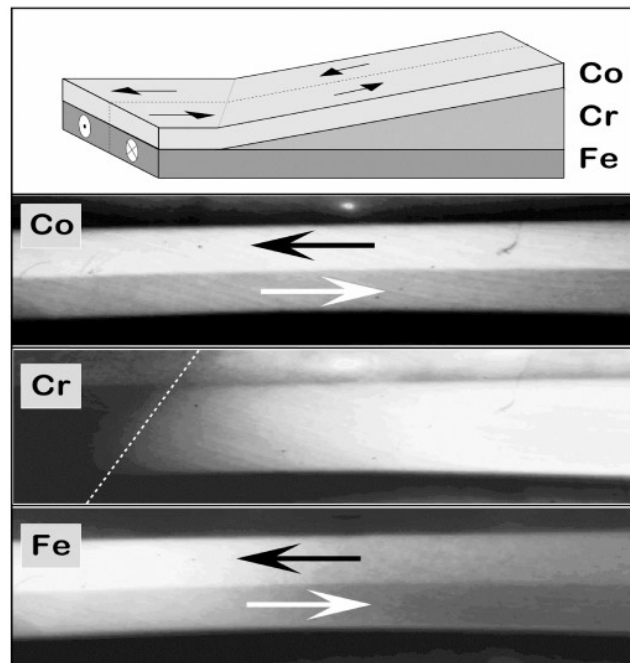
(a)

Figure 8. Investigation of the magnetic exchange coupling between Fe and Co across a Cr wedge prepared at slightly elevated temperature (a) and at 500 K (b). On an Fe(100) whisker a Cr wedge was grown and covered with 5 ML Co. The thickness of the Cr wedge increases from left to right from 0 to 10 ML (a) or 0 to 3 ML (b) as indicated in the top panel. For technical reasons the orientation of the Cr wedge is tilted with respect to the Fe whisker (see the dashed line). The element-resolved domain images for Co, Cr and Fe have been taken at the corresponding L_3 absorption edges. Note the change of the magnetic coupling between Fe and Co at a Cr thickness of ∼2 ML and the magnetic contrast visible in the Cr image in (b) (from [86] and [93], for (a) and (b), respectively).

way. The Cr wedge with increasing thickness from 0 to 10 monolayers (ML) was grown on an Fe(100) whisker (single crystal) surface. Finally the whole structure was covered by a 5 ML Co film. The film structure is schematically illustrated in the top panel. This sandwich system was imaged element selectively at the L_3 edges of Co, Cr and Fe. These images are obtained in the 'survey mode' with the objective lens being operated as an electrostatic triode. The survey mode is characterized by a low voltage of the extractor electrode, cf figure 1. In this mode, a field of view as large as 0.7 mm is possible with a corresponding resolution of about 1 μm. The typical domain structure of the Fe whisker, two regions of opposite magnetization, is clearly visible in these single images without magnetic contrast enhancement. Bright areas correspond to a magnetization direction opposite to the direction of photon incidence and dark areas to magnetization along the photon incidence. This simple domain configuration often encountered in Fe whiskers is very convenient for imaging magnetic coupling phenomena in wedge-shaped overlayers [99–101].

In figure 8(a), obtained at the PM3 of BESSY I for the preparation at *slightly elevated temperatures* [86], the decrease of brightness and contrast in the Fe image (bottom) from left to right is a consequence of the degradation of the signal due to the increasing thickness of the top layers. Nevertheless, the magnetic structure is clearly visible through 10 ML Cr plus 5 ML Co, i.e. a total thickness of almost 5 nm. The Cr-selective image shows the onset (dashed line) and increase of the Cr wedge. In figure 8(a), a domain structure in Cr is not visible on this length scale (field of view 500 μm diameter), even with magnetic contrast enhancement. Finally, the Co-selective image shows the domain structure in the Co top layer. Interestingly,
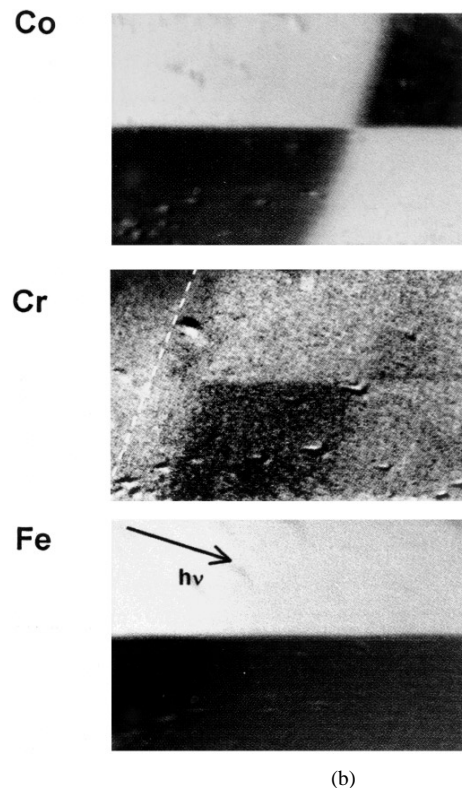

(b)

Figure 8. (Continued)

in this case the Co layer is coupled ferromagnetically to the substrate all along the Cr wedge.

A different behaviour arises if the deposition of the Cr wedge and Co top layer is performed at *higher substrate temperatures: here at 500 K*. Figure 8(b) shows the element-specific domain patterns in this case, investigated by Kuch *et al* [93]. The plane of incidence was oriented along the whisker. These images were taken at the ESRF with total exposure times of about 5 min for each helicity, thanks to the high brightness of the undulator beamline ID 12 B [82].

The bottom image of figure 8(b) again shows the domain structure of the iron whisker seen through the Cr and Co layers. It exhibits the same domain configuration of two oppositely magnetized domains aligned parallel to the whisker as discussed in figure 8(a). In this case, however, the Co and Cr domains look different. The Cr thickness varies from 0 to about 3 ML across the field of view. Again, the onset of the Cr wedge is tilted for technical reasons as indicated by the dashed line in the centre image. The Co image (top) reveals that up to a certain thickness of the Cr wedge the Co magnetization is *parallel* to the Fe magnetization. For a Cr thickness above about 2 ML the magnetic contrast in the Co image is reversed with respect to the Fe image. At these Cr thicknesses, Co obviously displays an *antiferromagnetic* coupling to the Fe substrate. Close to the transition from ferromagnetic to antiferromagnetic coupling, a small region with an intermediate grey level is observed. This could be due to a simultaneous presence of ferromagnetic and antiferromagnetic coupling in that region, or to a biquadratic coupling behaviour, which would result in a $90°$ rotation of the Co magnetization [102].

The element selectivity of the method allows us to study the residual ferromagnetic ordering of the Cr wedge induced by the adjacent Fe and Co magnetic layers. The centre image of figure 8(b) shows the residual magnetization of Cr with the photon wavelength being tuned to the Cr L_3 edge. Unlike figure 8(a), in this case there is indeed a net ferromagnetic moment also in the Cr layer. The Cr magnetization obviously follows that of the Co top layer. A darker grey level occurs in the lower half of the image in the centre region and in the upper half on the right-hand side. Only at the lowest Cr coverages below about 0.3 ML, just right of the broken line, the Cr magnetization appears to be opposite to that of Fe and Co. A similar behaviour has been observed for submonolayer Cr wedges on Fe(100) without additional overlayers, in the case where the Cr is deposited at room temperature [103]. The comparison of figures 8(a) and (b) suggests that in such exchange-coupled systems the preparation conditions play a crucial role. From these results it becomes clear that elemental selectivity is an absolute prerequisite for studying the coupling behaviour of sandwich-like structures on a ferromagnetic surface.

By comparison of these results with those observed for the Fe/Cr/Fe system, where the switching to antiferromagnetic exchange coupling occurs at 4–5 ML [99, 101], Kuch *et al* [93] conclude that different magnetic layers may influence the phase in the magnetic coupling. The difference in the Cr switching thickness could thus be attributed to a phase shift in the oscillations in the exchange coupling due to the different matching of the electronic states of Co and Cr as compared with Fe and Cr. A significant influence of the amount of interface intermixing on the occurrence of the antiferromagnetic interlayer coupling [104] may also play a role. Whereas the period of the oscillation in the interlayer exchange coupling depends only on the non-ferromagnetic interlayer material, different magnetic layers seem to influence the phase [105, 106].

The MXCD asymmetry (cf equation (9)) at the Cr L_3 edge in figure 8(b) is only 0.3–0.5% in contrast to about 20% at the Fe or Cr L_3 edges. This indicates that the total moment of the Cr layer is much lower than the Fe or Co moments. Furthermore, the asymmetry visible in the Cr image is weaker in the region of the antiferromagnetic coupling (right-hand side of the image). This can be explained by the fact that the contributions at the Fe–Cr and Cr–Co interfaces tend to cancel out in the antiferromagnetic coupling region, whereas they add up in the region of ferromagnetic coupling. Kuch *et al* [93] draw further conclusions on the relative

coupling strengths and the effect of a possible interface roughness.

The magnetic coupling of a *sub-monolayer Cr wedge to an Fe(100) crystal surface* has been investigated by Schneider *et al* [86]. This experiment also gives information about the sensitivity of the PEEM method. A result in shown in figure 9. The Cr films were grown as discontinuous wedges forming a sequence of equidistant terraces of 10 μm width per terrace. The Cr coverage was increased stepwise by 0.1 ML increment, as indicated by the numbers in the top panel. The chemical contrast taken at the Cr L_3 edge clearly reflects this stepwise increase of coverage (top panel). The image of the dichroism asymmetry in the Cr L_3 signal (centre panel) reveals a magnetic contrast of Cr which is the same as the domain pattern of the Fe substrate (bottom panel). Obviously, the domain structure in the Cr film results from a ferromagnetic coupling to the Fe substrate over the whole coverage range shown. The maximum magnetic contrast in the Cr image is only about 0.8% MXCD asymmetry. Despite this fact it was possible to discern the magnetic contrast even at the smallest film thickness of 0.1 ML. For a preparation at room temperature, Schneider *et al* [103] have found a different behaviour with the Cr–Fe coupling character changing from ferromagnetic to antiferromagnetic in this submonolayer coverage range. Again, the behaviour of the exchange coupling critically depends on the preparation conditions. The reasons may be found in the formation of a Cr–Fe interfacial alloy or in two-dimensional cluster formation depending on growth temperature.
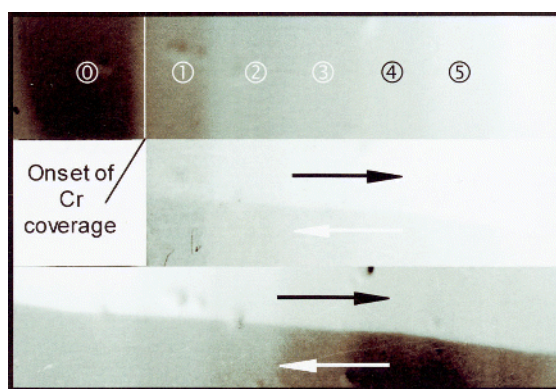

Figure 9. Analysis of a stepped sub-monolayer structure of Cr on Fe(100) deposited at elevated temperature. The chemical and magnetic contrast of Cr is depicted in the top and centre panel, respectively. The domain structure of the Fe whisker is given in the bottom panel (from [86]).

Another interesting coupling phenomenon in a *cobalt–nickel sandwich structure*, also observed by Kuch *et al* [93], is shown in figure 10. Co squares of 8×8 μm^2 were grown epitaxially on a Cu(100) single crystal surface at a thickness of 15 ML. This magnetic structure was covered by an Ni film of 8 ML thickness. The element-selective magnetization patterns of Co and Ni were taken by tuning the photon energy to the corresponding L_3 edges of the two elements. The Co image has already been discussed in figure 6(c). With one exception (bottom left square) the Co squares appear in single-domain states characterized by an in-plane magnetization. In the 'as-grown' state some squares appear with a positive projection of magnetization on the direction of the photon spin (bright), others with a negative projection (dark). The two equivalent easy in-plane axes cannot be distinguished in this experiment.

The Ni image shows a more complicated domain behaviour. In the region of the Co squares the same pattern as in the Co image is seen, characterized by the three dark squares. In the Co-free region (right part of the image) a faint domain pattern with irregularly shaped domain walls is visible in the Ni image. This pattern is characteristic for a magnetic layer with
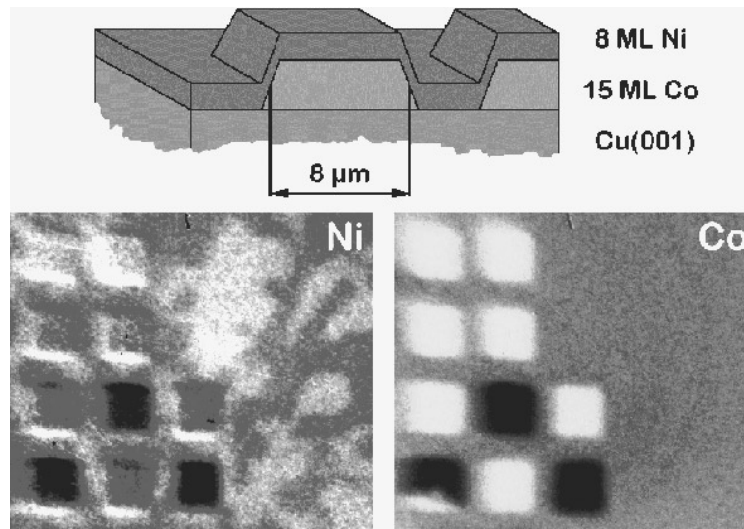
Figure 10. Element-resolved domain structure of a micro-patterned epitaxial Ni/Co film. A 15 ML thick square array (8×8 μm^2) of Co on Cu(100) was coated with 8 ML of Ni. On top of the Co squares the Ni layer couples ferromagnetically to the in-plane magnetization of Co. In contrast, in the Co-free region (right half of the images) a magnetic structure with rounded domain walls appears in the Ni image, indicative of an out-of-plane magnetization. Since the projection of the photon spin onto the surface normal is smaller at 65° angle of incidence, the contrast in the out-of-plane magnetized domains is smaller than for the in-plane domains (from [93]).

a magnetization vector perpendicular to the film plane.

The principal behaviour can be understood looking at the top panel of figure 10. The in-plane anisotropy forces the magnetization vector of the Co squares into the film plane. Via exchange coupling the 8 ML Ni film couples ferromagnetically to the Co in the same orientation. In the Co-free regions, however, an Ni film in this thickness range exhibits a perpendicular magnetization, as observed in other measurements [107, 108]. The photon beam is oriented at almost grazing incidence (25°) with respect to the surface. The projection of photon spin s_γ onto the in-plane magnetization $M_\parallel$ is thus larger (proportional to $\cos 25° = 0.91$) than the projection on the perpendicular magnetization $M_\perp$ (proportional to $\cos 65° = 0.42$). Consequently, the magnetic contrast for regions with in-plane magnetization is larger than for perpendicular magnetization.

4. Lorentz contrast in photoemission microscopy

4.1. Origin of the Lorentz-type contrast

In this mode of magnetic imaging using a PEEM the magnetic contrast arises due to the presence of a magnetic stray field in the surface region of the sample. This method is not element specific but it has the important practical advantage that no special light source like a synchrotron is required. It can be performed with simple laboratory UV lamps.

The Lorentz force acting on a moving charge in a magnetic field causes a deflection of the trajectories. The resulting contrast in the electron microscope is therefore called Lorentz contrast. It arises in transmission and scanning electron microscopy (TEM and SEM, respectively) and is utilized for magnetic imaging (for details see e.g. [109, 110]). Lorentz

contrast in a TEM arises due to the deflection of the electron beam usually inside a magnetic material. In a SEM two different types of Lorentz contrast can occur. The so-called type I contrast arises in the secondary electron image and results from the action of the external magnetic stray field. The type II contrast occurs around certain impact angles inside the material in the case when the elastically backscattered electrons are detected. For the case of a PEEM the effect of stray fields close to the sample surface resembles the type I contrast. For a collection of experimental and theoretical data see the recent review by Nepijko *et al* [111].

Figure 11 illustrates the origin of the Lorentz contrast in PEEM. In this case we assume the magnetic stray field to point out of the plane of the drawing in the left half of the sample and into the plane of the drawing in the right half. In the simplest case (spherically symmetric initial state) the angular distribution of the photoelectrons is given by a cos Θ distribution. Θ is the angle between the emission direction and the surface normal of the sample. The magnetic stray field essentially causes a rotation of this angular distribution either clockwise or anticlockwise, depending on the local direction of the magnetic stray field. As discussed in section 2, the contrast aperture in the backfocal plane of the objective lens selects the solid angle interval of the electron emission distribution contributing to the image. If the contrast aperture is placed off-centre as shown in the figure, a magnetic contrast arises. In one region the maximum of the angular distribution is selected (here the right part of the sample), whereas for the opposite stray field direction (left part) a region significantly outside the maximum is
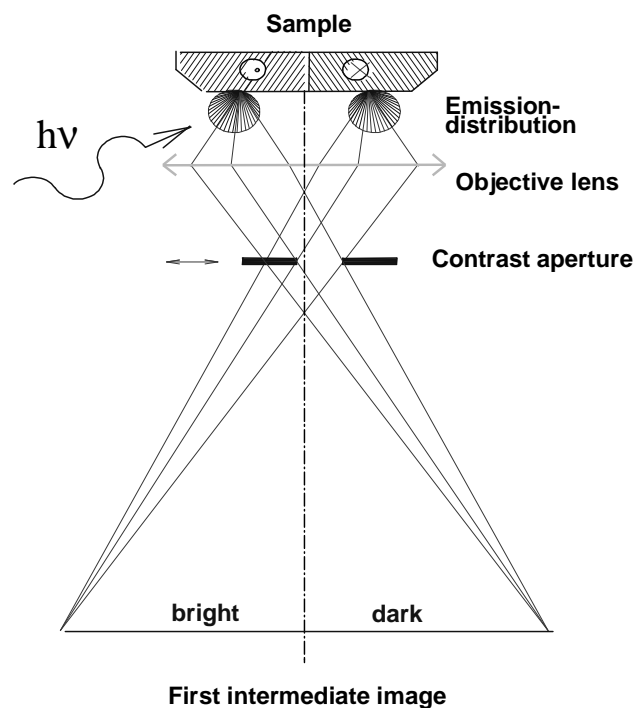

Figure 11. Origin of the Lorentz contrast due to stray magnetic fields close to the surface. The change of electron trajectories due to the Lorentz force leads to a rotation of the electron emission distribution, either clockwise or anticlockwise, depending on the local stray field perpendicular to the plane of the drawing. With an asymmetric position of the contrast aperture the rotation of the emission distribution can be exploited for a magnetic contrast.

selected. Consequently for the situation shown in figure 11 the right part of the sample will appear brighter than the left part.

It can be shown [111] that a weak magnetic stray-field contrast arises even when no contrast aperture is used. This appearance of a Lorentz-force-based contrast was discovered as early as 1957 by Spivak *et al* [11]. More recently Mundschau *et al* [27] exploited the Lorentz-type contrast for magnetic imaging.

4.2. Application for hard-magnetic materials

Figure 12 shows an example for the Lorentz contrast for NdFeCu, a hard magnetic material with high coercive force investigated by Marx *et al* [112]. In several regions regular patterns of striped domains with a typical period of about 2 μm are visible. In the right panel a line scan through one of the regions is plotted. This result is characteristic for a domain structure with periodically changing magnetization direction. In addition, the surface region shows a topographical contrast, i.e. scratches and defects as well as an indication for different chemical phases.
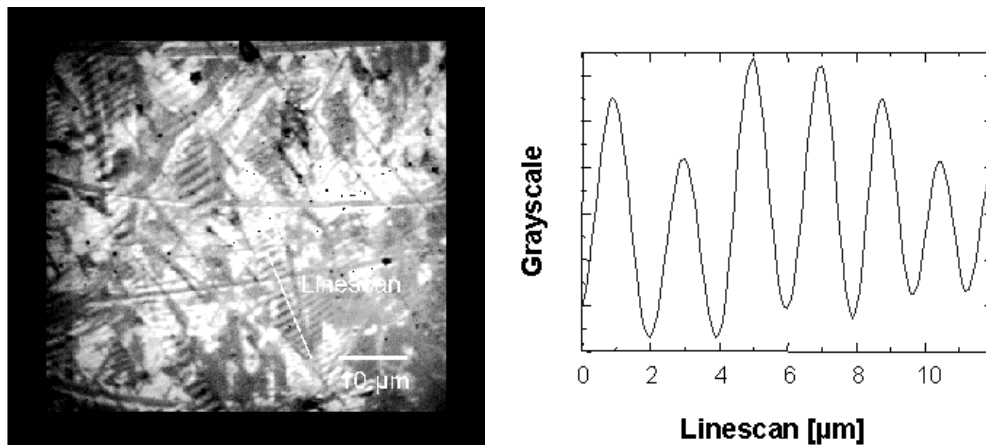

Figure 12. Lorentz contrast in the PEEM image of a hard-magnetic NdFeCu sample. The periodic striped domains visible in the image and in the line scan result from the action of the Lorentz force on the electron trajectories. The image was taken using a UV laboratory light source (from [112]).

Marx *et al* present a detailed treatment of the origin of the observed contrast assuming an array of regularly striped domains. Nepijko *et al* [111] treat various cases of different geometries of domains and domain walls in an analytical theory. Since the stray fields decay only gradually with increasing distance from the surface (depending on the domain size), the lateral resolution is limited to typically 300 nm for realistic cases [112].

Besides the imaging of domain structures this method is also suitable to detect magnetic stray fields of building elements such as sensors or write/read heads for magnetic storage media. Its major advantage is that it does not require a special light source since the contrast is maximum for the lowest-energy electrons in threshold emission (UV-PEEM).

5. Magnetic contrast in threshold photoemission microscopy in analogy to the magneto-optical Kerr effect

5.1. Origin of the Kerr-effect-like contrast

The third and most recent achievement of magnetic imaging using PEEM was discovered by Marx *et al* [113]. Like the Lorentz-type contrast is arises in threshold emission but its origin lies in the existence of the local magnetization *inside* the magnetic material. It can be discussed in the framework of the magneto-optical Kerr effect. This effect results from a dependence of the dielectric tensor ε on the magnetization of the sample. The Kerr effect causes a small rotation of the electric vector upon reflection on the sample surface as well as a magnetization-dependent intensity modulation of the reflected light beam in a special geometry. Depending on the relative orientation of magnetization and plane of incidence one can distinguish between longitudinal ($M \parallel$ plane of incidence) and transversal Kerr effect ($M \perp$ plane of incidence). Optical Kerr microscopy is to date the most common technique for magnetic domain imaging [42]. It employs light in the visible or near-UV range. Its lateral resolution is diffraction limited. By using an immersion objective lens and an optimized dielectric coating of the magnetic sample surface resolutions down to about 300 nm can be achieved in favourable cases. In contrast, photoemission microscopy is characterized by a base resolution in the region of 20 nm.

In section 3 we have discussed that imaging of magnetic domain patterns with PEEM is possible using circularly polarized synchrotron radiation and exploiting magnetic circular dichroism. This dichroism effect occurs at characteristic absorption edges and hence the approach depends on the access to a tunable light source in the soft x-ray range (X-PEEM). In threshold photoemission (UV-PEEM) the photon energy is only slightly larger than the workfunction. Consequently, only electrons in a narrow energy window of typically less than 1 eV can contribute to the image. In this case, the amount of inelastically scattered secondary electrons is small and the entire spectrum is dominated by direct photoelectrons. In addition, due to their low kinetic energy the excited electrons are strongly refracted upon leaving the crystal. Therefore, the image is formed by electrons having only a small wave-vector component $k_\parallel$ parallel to the surface, i.e. total momenta close to the normal emission condition.

We will explain the origin of the magnetic contrast by using a simple model known from the description of the transversal magneto-optical Kerr effect (see figure 13). In a magnetized sample the dielectric response to the external electric field vector has two main contributions. The first is the refraction at the solid–vacuum interface leading to an orientation of the transmitted dielectric vector D_t more parallel to the surface as compared with the electric vector E_i of the incident light wave outside the material.

Second, the Lorentz force acts on the quasi-free metal electrons leading to a small additional rotation (the Kerr rotation θ_k) of the dielectric vector D_{t+k} as schematically illustrated in figure 13. This rotation is the origin of the magneto-optical Kerr effect (intensity modulation in the reflected photon beam with electric vector E_r) [114]. It also gives rise to the magnetic contrast discussed in this section. Since the photoelectrons contributing to the image have momenta in a small solid angle interval around the z-axis (surface normal n), the projection of the dielectric vector D_{t+k} onto the z-axis is a measure of the transition amplitude of the emitted electron signal. Threshold photoemission has been treated e.g. by [115–117]. In the simple picture of quasi-free electrons, i.e. neglecting all band-structure effects, the emission intensity I along the direction z is proportional to the square of the scalar product
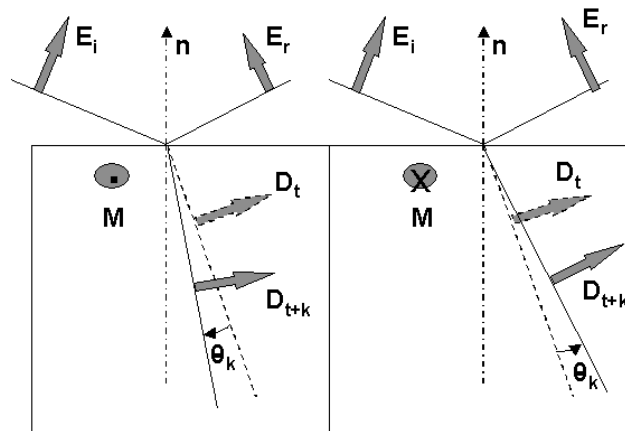
$$I \propto (D \cdot z)^2 \tag{10}$$

Figure 13. Origin of the Kerr-effect-like magnetic contrast in threshold photoemission. The phenomenon arises in the geometry used to measure the transversal magneto-optical Kerr effect and has the same origin. The angle of Kerr rotation is enlarged to illustrate the principle.

In figure 13 we have assumed a magnetization vector perpendicular to the plane of the drawing and pointing upwards in the left-hand domain (M^+) and downwards in the right-hand domain (M^-). The resulting rotation of the dielectric vector is thus clockwise or anticlockwise, respectively. In the case of the anticlockwise rotation the projection of D_{t+k} onto the z-axis is *larger*, thus giving rise to a *higher* photoelectron intensity normal to the surface than in the opposite case. The corresponding domain (right) will therefore appear *brighter* than the other one. Marx *et al* [113] treat the realistic case of a finite solid angle of emission and take into account metal optics. The schematic principle of figure 13 illustrates that the orientation of the magnetization vector on the right-hand side leads to an enhanced photoelectron signal and also to *a larger reflected intensity* as compared to the left-hand side in the optical Kerr signal determined by $|E_r|^2$. More details of this analogy are discussed in [113].

5.2. Magnetic linear dichroism in the photoelectron angular distribution

The simple picture of quasi-free electrons being essentially based on the Drude theory extended for the presence of a sample magnetization is particularly useful for polycrystalline materials, where no k-resolution is given. For the case of single-crystal surfaces the microscope detects electrons around a well defined direction in k-space. In this case the so-called magnetic linear dichroism in the angular distribution (MLDAD) [118] must be considered. Such magnetization-dependent intensity differences in photoemission with linearly polarized (and unpolarized) light have been observed in spectroscopy experiments for various magnetic materials both in the x-ray range [119], and in VUV photoemission [120–122].

Henk and Feder [123] have performed *ab initio* photoemission calculations for the Ni(110) surface at $h\nu = 5.1$ eV photon energy. In a group-theory-based analytical approach they treat the photo-excitation in a fully relativistic electron system. This treatment indeed predicts the existence of a magnetic dichroism in particular for sp-polarized light, i.e. with the electric vector being rotated by $45°$ in comparison to the situation depicted in figure 13. This type of MLDAD occurs even without inclusion of the surface optical response, i.e. it is of different origin from the Kerr-effect-like contrast discussed above. The theoretical description is hampered by the fact that, as in most fcc materials, the accessible final states in Ni threshold photoemission fall

into a bulk band gap. The electrons are therefore excited into *evanescent final states* which decay exponentially in the bulk. Such a situation can be properly described only in a one-step treatment of the photoemission process.

The model calculation [123] used the framework of the formalism which had previously been successfully applied to the analysis of magnetic linear and circular dichroism in Ni [124, 125]. It accounts for the optical response of the surface on the basis of Fresnel's equations. Since we are primarily interested in the microscopic origin of the magnetic dichroism with linearly polarized light, the example of an in-plane magnetized Ni(110) surface has been chosen. Indeed, this model calculation reveals a substantial magnetic dichroism asymmetry as illustrated in figure 14. The photoemission spectra (figure 14(b)) vary strongly with the orientation of M. In particular, the spectra with M parallel to the crystal mirror planes [010] (x) and [011] (y) differ significantly from each other. This is due to the uniaxial asymmetry of the magnetic {110} surface which is reflected in the relativistic wave functions and shows up clearly in the layer-resolved density of states (LDOS) (see the bottom panel). Most of the spectral features can be directly related to peaks in the bulk LDOS (figure 14(a)). This calculation has been carried out for sp polarization, i.e. the electric vector being rotated by $+45°$ or $-45°$ with respect to the plane of incidence (+sp or −sp, respectively). The photon
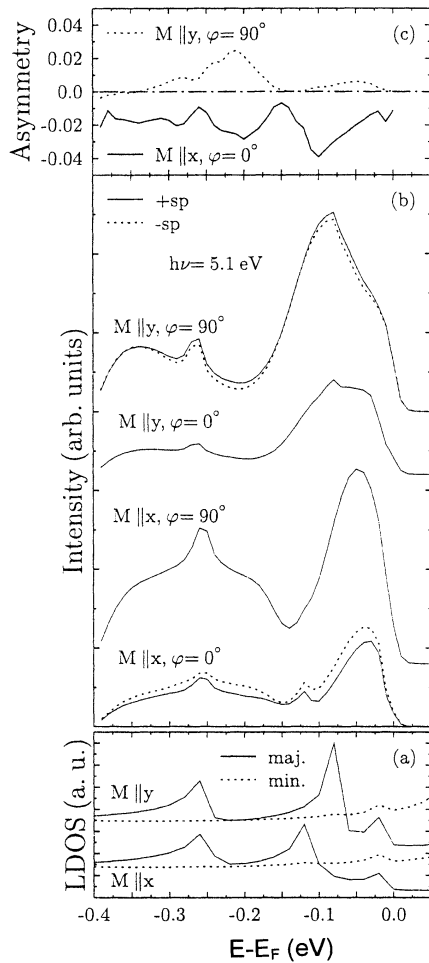

Figure 14. Linear magnetic dichroism in threshold photoemission from the Ni(110) surface in a fully relativistic photoemission calculation: (a) layer-resolved density of states; (b) normal emission photoelectron spectra for an in-plane magnetization M along one of the two mirror planes x and y, for perpendicular direction of light incidence $\Phi = 0°$ and $\Phi = 90°$; (c) magnetic dichroism spectra (from [123]).

energy was $h\nu = 5.1$ eV. For the sp-polarized light the dichroic signal disappears whenever M is perpendicular to the plane of incidence ($M \parallel y$, $\Phi = 0°$; $M \parallel x$, $\Phi = 90°$).

Unlike the case of the simple model discussed above, here a non-zero dichroism requires a component of M along the photon wave vector q. The MDAD signals for $M \parallel x$ and $M \parallel y$ differ not only in magnitude but also in sign (figure 14(c)). It is important to note that each MDAD spectrum does not change sign within a 0.5 eV interval below E_F. An energy integration over this interval therefore results in a magnetic dichroism with different magnitude and opposite sign orientations of M. In conclusion, the fully relativistic photoemission calculation for the Ni(110) surface in close-to-threshold photoemission predicts a substantial dichroism asymmetry of the order of several per cent, which should show up as magnetic contrast in the PEEM images.

5.3. First experimental results

Marx *et al* [113] have performed the first experiments to detect the novel magnetic contrast mechanism in threshold photoemission. The experimental geometry corresponds to a typical arrangement for detecting the transversal Kerr effect with an angle of photon incidence of 75° with respect to the surface normal. The photon beam from an Xe–Hg high-pressure arc lamp ($h\nu \leqslant 5.2$ eV) passed through a linear polarizer (Glan–Thompson prism) and was focused onto the sample surface. By rotating the prism the linear polarization could be changed continuously between s- and p-polarized states.

A polycrystalline iron film with a thickness of 100 nm has been deposited by means of UHV evaporation onto an Si wafer with native oxide layer. The sample holder allowed the *in situ* application of an external magnetic field. The coercive field of the iron film was determined to be about $\mu_0 H = 4$ mT. The workfunction of the film was about $\Phi = 4.8$ eV, so that the energy width of the photoelectron distribution was approximately $\Delta E \leqslant 0.4$ eV.

In section 3 it has been shown that the magnetic contrast can be enhanced by subtracting a suitable 'background image'. In threshold photoemission this background image can be taken with either a completely demagnetized or a fully magnetized sample, a technique which is also used in Kerr microscopy [42]. In the resulting difference image, other contrast contributions such as workfunction contrast, topographical contrast, impurities etc are largely eliminated. Figure 15 shows an example of the resulting magnetic contrast observed [113]. In this case a background image of the sample in a demagnetized state has been subtracted. The asymmetry value extracted from regions of opposite magnetization is $A_{MLDAD} = (0.37 \pm 0.10)\%$. Quantitatively, this asymmetry agrees well with the corresponding value for the magneto-optical Kerr effect measured for Fe [126, 127].

Figure 15 shows a series of images taken during a magnetization procedure. After initial demagnetization with an AC field the film has been exposed to a field of 2.72 mT. Then, the upper left image has been taken in zero field. Next, a field of 2.79 mT has been applied, yielding the second image, and so on. In this way, the stepwise growth of the bright domains (M pointing to the right) became visible.

As compared to the demanding experimental requirements of circularly polarized tunable radiation in the soft x-ray range, the novel approach is extremely simple. It works with a *standard laboratory UV source*. If we take into account that unpolarized light contains a 50% contribution of p-polarization (which could be enhanced inside the material due to metal optics) the mechanism described in figure 13 should also exist for unpolarized light. Indeed, Marx *et al* [113] were able to image the magnetic domains in the polycrystalline iron film using unpolarized light (see figure 16). In this case the magnetic asymmetry is $A = 0.18\%$, i.e. about half of the value obtained for linearly polarized light. The field of
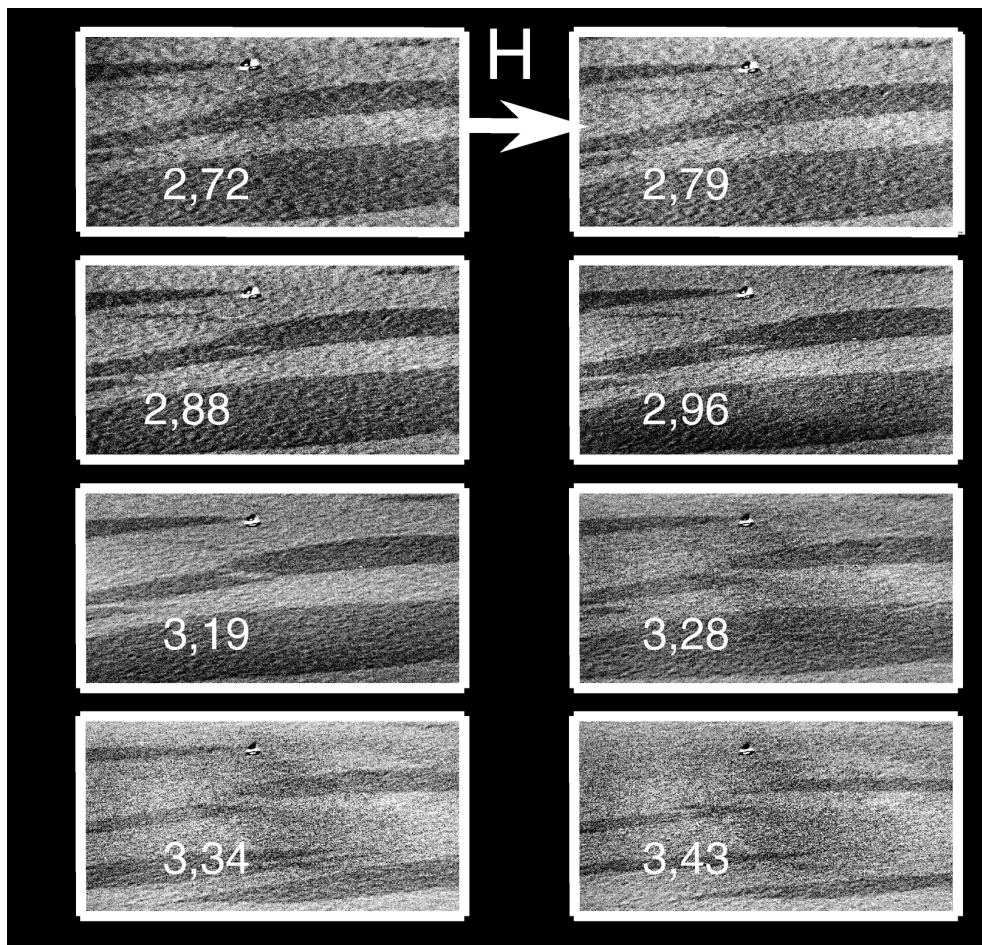
Figure 15. Domain structure of a polycrystalline Fe film after application of an external magnetic field (stepwise increased, field given in mT). The images were taken using a UV laboratory source in the geometry of figure 13. The magnetic contrast arises as a consequence of the magnetization-dependent Kerr rotation of the dielectric vector inside the magnetic material (from [113]).

view is about $150 \times 150 \ \mu\text{m}^2$ at a resolution of the CCD camera of 1024×1024 pixels. The total exposure time was 120 s. In the future, the difference image will be obtained by using two photon sources placed symmetrically with respect to the surface normal. Upon switching between the two light sources the magnetic contrast will be reversed. Then, there is no need to change the magnetization of the sample to take a background image and the magnetic contrast will be enhanced by a factor of two. In principle, a second pair of lamps placed in the azimuth perpendicular to the first one allows us to probe the second in-plane component of M.

If we compare the information content of the Lorentz contrast (section 4) and the Kerr-effect-like contrast of this section, there are important differences. The Lorentz contrast is based on the existence of an external magnetic stray field close to the sample surface. Therefore, the method is well suited for perpendicularly magnetized structures and for the observation of domain walls. A uniform in-plane magnetization of a thin film will generally not lead
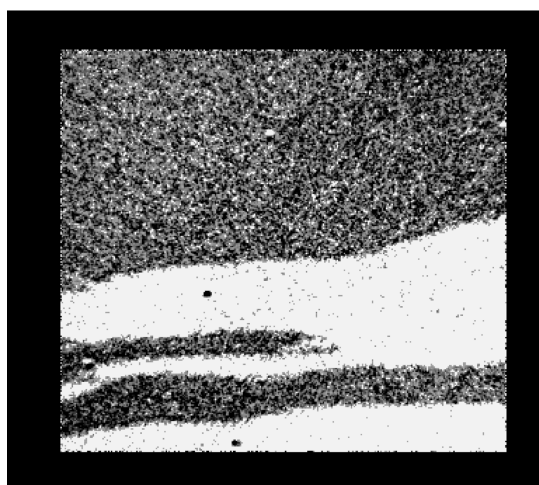
Figure 16. Domain pattern of a polycrystalline Fe film obtained with unpolarized UV light (from [113]).

to a contrast. A thin-film structure (such as a square) which is uniformly magnetized will essentially show up in the regions of the magnetic poles. In this respect the technique bears much resemblance to magnetic force microscopy. In contrast, optical Kerr microscopy as well as its counterpart in photoemission microscopy yield a true domain contrast. In this case the phenomenon arises inside the material. A thin-film structure that is uniformly magnetized will appear in a uniform grey level.

Although the first results have been measured for thin Fe films, the phenomenon has the same general physical origin as the magneto-optical Kerr effect. It will thus not be restricted to a specific class of materials. Due to its potential for high lateral resolution and the efficient parallel image acquisition, the new technique is highly attractive for applications. It is a relatively simple laboratory method and does not require special light sources such as synchrotron radiation.

6. Conclusions and outlook

After about a decade of intense development the imaging of magnetic structures using photoemission electron microscopy (PEEM) has proven to be a powerful tool. Especially in combination with tunable circularly polarized radiation in the soft x-ray range from electron storage rings the method can exhibit its full potential. Exploiting the *magnetic x-ray circular dichroism* (MXCD) the magnetism and domain structure of homogeneous samples as well as selected micro- and nanostructures can be investigated. The striking advantage of MXCD-PEEM becomes obvious especially in the study of magnetic coupling phenomena in a laterally resolved way. Selection of element-specific x-ray absorption edges allows the mapping of buried layers and microstructures. The interlayer exchange coupling between different magnetic materials across non-magnetic spacers becomes directly visible. Also an induced magnetization in the spacing material can be detected as shown for the case of the wedged Co/Cr/Fe sample. In the *microspectroscopy mode* the magnetic dichroism signal of a selected spot on the sample can be measured. In the *spectromicroscopy mode* the magnetic dichroism asymmetry is used to generate the magnetic contrast in an image. Since the PEEM acquires the

image in a parallel way, it is principally much faster than all scanning-beam or scanning-probe techniques. Its sensitivity allows the study of submonolayer coverages as shown for the Cr/Fe system. Furthermore, it gives access to the fine structure of domain walls.

The X-PEEM technique benefited greatly from the progress in *soft x-ray beamlines*. Up to now, most of the work has been performed at bending-magnet beamlines and/or synchrotron radiation sources of the second generation. The change to an undulator beamline at a third generation source will lead to an improvement of the brilliance by two to three orders of magnitude. Whereas images like those in section 3 required exposure times of typically a few minutes, we expect at BESSY II image sequences with the rate of seconds. This will facilitate the investigation of dynamical effects. If, in addition, the time structure of the synchrotron radiation is exploited, a time resolution in the range below 500 ps is possible. In a time-of-flight (TOF) mode of operation such time resolutions have already been obtained in TOF-PEEM [80, 81]. This can give direct access to processes of magnetization reversal and switching in devices of spin electronics. Chemical and magnetic microspot analysis (XANES and MXCD microspectroscopy) was possible with typical spatial resolutions of about 1 μm [34, 73]. The gain in brilliance should allow us to drive the spatial resolution of microspectroscopy down to the region below 100 nm.

Considerable improvements are also to be expected for the *electron optics of the microscopes*. The relatively simple instruments being in use can reach resolutions of about 10–20 nm [19, 34, 67, 128] in threshold photoemission, i.e. for a narrow energy distribution of the imaged electrons. For photon energies in the soft-x-ray range as necessary for the MXCD technique the resolution is diminished significantly. This is a direct consequence of the larger energy width of the secondary electron distribution which contributes to the image. Electron optically, the energy spread leads to a chromatic aberration. This aberration may be reduced in the future by using smaller contrast apertures. For reasons of intensity, however, this was not possible under most of the present experimental conditions (bending magnet beamlines).

The spatial resolution can be further enhanced by the insertion of elements which correct the spherical and chromatic aberrations. The action of such elements has been successfully proven in transmission electron microscopy [129–131]. A corrected PEEM/LEEM has been designed by Rose *et al* and is currently under construction [68]. Theoretically, resolutions below 1 nm are possible. In practice, however, topographical features as well as magnetic and electric stray fields (caused, e.g., by workfunction differences) lead to a considerable reduction of the obtainable resolution [69]. Recently, first experimental results aiming at a chromatic correction via the TOF technique have been obtained [80, 81]. In the future, the various possibilities of resolution enhancement will facilitate detailed investigations of very small chemical and magnetic structures as well as domain walls.

Two other modes of magnetic imaging using a PEEM do not require synchrotron radiation and are therefore highly attractive for standard laboratory applications. One exploits the electromagnetic forces experienced by the low-energy photoelectrons when leaving the sample. The resulting changes of the trajectories lead to a *Lorentz-type contrast*. This mode has been demonstrated by an example of a hard-magnetic material (NdFeCu). In fact, this oldest type of magnetic imaging via PEEM was discovered and investigated as early as 1957 by Spivak *et al* [11].

The third type of magnetic contrast in PEEM has been detected very recently by Marx *et al* [113]. It occurs in threshold PEEM in the geometry of the transversal magneto-optical Kerr effect. The magnetization-dependent rotation of the dielectric vector inside of the material gives rise to a *Kerr-effect-like contrast* in the PEEM image. The first experimental results have been obtained for polycrystalline iron films. There is, however, much evidence that the phenomenon has the same general nature as the magneto-optical Kerr effect itself. Owing to its

simplicity, its high resolution and the fact that it even works with unpolarized UV-light from a simple laboratory source, this novel method of magnetic imaging is very attractive. Therefore, a wide range of applications, in particular in the field of spin electronics, can be expected.

Acknowledgments

References

  [1] Brüche E and Johannson H 1932 *Z. Phys.* **33** 898
  [2] Brüche E 1933 *Z. Phys.* **86** 448
  [3] Brüche E 1942 *Kolloid. Zeitschr.* **100** 192
  [4] Recknagel A 1941 *Z. Phys.* **117** 689
  [5] Recknagel A 1943 *Z. Phys.* **120** 331
  [6] Möllenstedt G and Düker H 1953 *Optik* **10** 192
  [7] Möllenstedt G and Lenz F 1963 Electron emission microscopy *Advances in Electronics* vol 13 (New York: Academic) p 251
  [8] Bethge H, Eggert H and Herbold K 1958 *3rd Int. Congr. on Electron Microscopy (Berlin)* vol I ed W Bargmann *et al* (Berlin: Springer) p 217
  [9] Bethge H and Heydenreich J (eds) 1982 *Elektronenmikroskopie in der Festkörperphysik* (Berlin: Springer) ch 8
[10] Bethge H, Krajewski T and Lichtenberger O 1985 *Ultramicroscopy* **17** 21
      Bethge H and Klaus M 1983 *Ultramicroscopy* **11** 207
[11] Spivak G V, Dombrovskaya T N and Sedov N N 1957 *Dokl. Akad. Nauk SSSR* **113** 78
[12] Spivak G V *et al* 1957 *Sov. Phys. Dokl.* **2** 120 (in Russian)
      Spivak G V and Lyubchenko 1959 *Izv. Akad. Nauk SSSR Ser. Fiz.* **23** 697
[13] Koch W 1958 *Z. Phys.* **152** 1
[14] Schwarzer R A 1981 *Microsc. Acta* **84** 51
[15] Düker H 1964 *Acta Phys. Austriaca* **18** 232
[16] Wegmann L 1969 Photoemissions-Elektronenmikroskopie *Handbuch der zerstörungsfreien Materialprüfung* ed E A W Müller (Munich: Oldenbourg) R.31,1
      Wegmann L 1972 *J. Microsc.* **96** 1
[17] Pfefferkorn G and Schur K (eds) 1979 *Beiträge zur elektronenmikroskopischen Direktabbildung von Oberflächen* **12/2** 1
[18] Grund S, Engel W and Teufel P 1975 *J. Ultrastruct. Res.* **50** 284
[19] Griffith O H and Rempfer G F 1987 *Adv. Opt. Electron Microsc.* **10** 269
[20] Rempfer G F, Skoczylas W P and Griffith O H 1991 *Ultramicroscopy* **36** 196
[21] Griffith O H and Engel W (eds) 1991 *Ultramicroscopy* **36** Nos 1-3
[22] Telieps W and Bauer E 1985 *Ultramicroscopy* **17** 57
[23] Mundschau M, Bauer E and Swiech W 1988 *Surf. Sci.* **203** 412
[24] Bauer E 1991 *Ultramicroscopy* **36** 52
[25] Bauer E 1994 *Rep. Prog. Phys.* **52** 895
[26] Veneklasen L H 1992 *Rev. Sci. Instrum.* **63** 5513

[27] Mundschau M, Romanowicz J, Wang J Y, Sun D L and Chen H C 1996 *J. Vac. Sci. Technol.* B **14** 3126–30
Mundschau M, Romanowicz J, Wang J Y, Sun D L and Chen H C 1998 *Surf. Rev. Lett.* **5** 1269–74
[28] Seve L, Sinkovic B and Zhu W 1999 *Appl. Phys. Lett.* submitted
[29] Schneider C M, Frömter R, Ziethen Ch, Schönhense G and Kirschner J 1997 *Synchr. Rad. News* **10** 22
[30] Ade H (ed) 1997 *J. Electron Spectrosc. Relat. Phenom.* **84** Nos 1–3
[31] Bauer E (ed) 1998 *Surf. Rev. Lett.* **5**
[32] Tonner B P, Dunham D, Zhang J, O'Brien W L, Samant M, Weller D, Hermsmeier B D and Stöhr J 1994 *Nucl. Instrum. Methods* A **347** 142
[33] Hillebrecht F U, Spanke D, Dresselhaus J and Solinus 1977 *J. Electron Spectrosc. Relat.* **84** 189
[34] Ziethen Ch, Schmidt O, Fecher G H, Schneider C M, Schönhense G, Frömter R, Seider M, Grzelakowski K, Merkel M, Funnemann D, Swiech W, Gundlach H and Kirschner J 1998 *J. Electron Spectrosc. Relat. Phenom.* **88–91** 983
[35] Fecher G H, Hwu Y and Swiech W 1997 *Surf. Sci.* **377–9** 1106–11
Swiech W, Fecher G H, Huth M, Schmidt O, Cheng N F, Lin C K, Tung C Y and Hwu Y 1998 *Appl. Phys.* A **67** 447–54
[36] Margaritondo G 1995 *Scann. Spectromicrosc.* **9** 949
Hwu Y *et al* 1995 *Nucl. Instrum. Methods* A **361** 349
Margaritondo G and Hwu Y 1996 *Appl. Surf. Sci.* **92** 273
Di Stasio G *et al* 1998 *Rev. Sci. Instrum.* **69** 3106
[37] For a review, see Imbihl R and Ertl G 1995 *Chem. Rev.* **95** 697
[38] Tonner B P and Harp G R 1988 *Rev. Sci. Instrum.* **59** 853
[39] Stöhr J, Wu Y, Hermsmeier B B, Samant M G, Harp G, Koranda S, Dunham D and Tonner B P 1993 *Science* **259** 658
[40] Kranz J and Hubert A 1963 *Angew. Phys.* **15** 220
[41] Schmidt F, Rave W and Hubert A 1985 *IEEE Trans. Magn.* **21** 1596
[42] Hubert A and Schäfer R 1998 *Magnetic Domains* (Berlin: Springer)
[43] Fuchs E 1960 *Naturwissenschaften* **47** 392
[44] Chapman J N 1984 *J. Phys. D: Appl. Phys.* **17** 623
[45] Zweck J, Chapman J N, McVitie S and Hoffmann H 1992 *J. Magn. Magn. Mater.* **104** 107
Zweck J, Zimmermann T and Schuhrke T 1997 *Ultramicroscopy* **67** 153
[46] Oepen H P and Kirschner J 1991 *Scanning Microsc.* **5** 1
[47] Unguris J, Celotta R J and Pierce D T 1991 *Phys. Rev. Lett.* **67** 140
Scheinfein M R *et al* 1990 *Rev. Sci. Instrum.* **61** 2501
[48] Koike K and Hayakawa K 1984 *Japan. J. Appl. Phys.* **23** L187
Koike K and Hayakawa K 1984 *Appl. Phys. Lett.* **45** 585
[49] Martin Y and Wickramasinghe H K 1987 *Appl. Phys. Lett.* **50** 1455
[50] Wadas A, Rice P and Moreland J 1994 *Appl. Phys.* A **59** 63
[51] Hehn M *et al* 1996 *Science* **272** 1782
[52] Wiesendanger R 1998 *Scanning Probe Microscopy* (Berlin: Springer)
[53] Kirz J, Jacobsen C and Howells M 1995 *Q. Rev. Biophys.* **28** 1
[54] Kirz J and Rarback H 1985 *Rev. Sci. Instrum.* **56** 1
[55] Warwick T *et al* 1998 *Rev. Sci. Instrum.* **69** 2964
[56] Fischer P *et al* 1996 *Z. Phys.* **101** 313
Fischer P *et al* 1998 *J. Phys. D: Appl. Phys.* **31** 649
[57] Prins M W J *et al* 1995 *Appl. Phys. Lett.* **66** 1141
[58] Betzig E, Trautmann J K, Wolfe R, Gyorgy E M, Flinn P L, Kryder M H and Chang C H 1992 *Appl. Phys. Lett.* **61** 142
[59] Bode M, Getzlaff M and Wiesendanger R 1998 *Phys. Rev. Lett.* **81** 4256
Wulfhekel W and Kirschner J 1999 *Appl. Phys. Lett.* **75** 1944
[60] Altman M S, Pinkvos H, Hurst J, Poppa H, Marx G and Bauer E 1991 *Mater. Res. Soc. Symp. Proc.* vol 232 (Pittsburgh, PA: Materials Research Society) p 125
[61] Pinkvos H, Poppa H, Bauer E and Hurst J 1992 *Ultramicroscopy* **47** 339
[62] Bauer E 1997 *Handbook of Microscopy* ed S Amelincks *et al* (Weinheim: VCH) pp 294, 487
[63] Duden T 1996 *PhD Thesis* TU Clausthal
Duden T and Bauer E 1995 *Rev. Sci. Instrum.* **66** 2861
Duden T and Bauer E 1996 *Phys. Rev. Lett.* **77** 2308
Duden T and Bauer E 1998 *Surf. Rev. Lett.* **5** 1213
[64] Stöhr J, Padmore H A, Anders S, Stammler T and Scheinfein M R 1998 *Surf. Rev. Lett.* **5** 1297

[65] Siegmann H C 1992 *J. Phys.: Condens. Matter* **4** 8395
[66] Schönhense G and Siegmann H C 1993 *Ann. Phys.* **2** 465–74
[67] Ade H, Yang W, English S L, Hartman J, Davis R F, Nemanich R J, Litvinenko V N, Pinayaev I V, Wu Y and
     Madey M J 1998 *Surf. Rev. Lett.* **5** 1257
[68] Fink R, Weiss M R, Umbach E, Preikszas D, Rose H, Spehr R, Hartel P, Engel W, Degenhardt R, Wichtendahl
     R, Kuhlenbeck H, Erlebach W, Ihmann K, Schlögl R, Freund H-J, Bradshaw A M, Lilienkamp G, Schmidt
     Th, Bauer E and Benner G 1997 *J. Electron Spectrosc. Relat. Phenom.* **84** 231
     Wichtendahl R *et al* 1998 *Surf. Rev. Lett.* **5** 1249
[69] Nepijko S A, Sedov N N, Schönhense G, Escher M, Xinhe B and Huang W submitted
[70] Chmelik J, Veneklasen L H and Marx G 1989 *Optik* **83** 5 155
[71] Glaser W 1952 *Grundlagen der Elektronenoptik* (Berlin: Springer) p 643
[72] Stöhr J 1992 *NEXAFS Spectroscopy (Springer Series in Surface Sciences 25)* (Heidelberg: Springer)
[73] Swiech W, Fecher G H, Ziethen Ch, Schmidt O, Schönhense G, Grzelakowski K, Schneider C M, Frömter R,
     Oepen H P and Kirschner J 1997 *J. Electron Spectrosc. Relat. Phenom.* **84** 171
[74] Hwu Y, Tsai W L, Chang L W, Chen C H, Wu C C, Noh D Y, Je J H, Fecher G H, Bertolo M, Berger H and
     Margaritondo G *Japan. J. Appl. Phys.* in print
[75] Bauer E, Koziol C, Lilienkamp G and Schmidt T 1997 *J. Electron Spectrosc. Relat. Phenom.* **84** 201
     Schmidt *et al* 1998 *Surf. Rev. Lett.* **5** 1287
[76] Tonner B P, Dunham D, Droubay T and Pauli M 1997 *J. Electron Spectrosc. Relat. Phenom.* **84** 211
[77] Marx G K L, Gerheim V and Schönhense G 1997 *J. Electron Spectrosc. Relat. Phenom.* **84** 251
[78] Schmidt O, Ziethen Ch, Fecher G, Merkel M, Escher M, Menke D, Kleineberg U, Heinzmann U and
     Schönhense G 1998 *J. Electron Spectrosc. Relat. Phenom.* **88–91** 1009
[79] Bostanjoglo O and Weingärtner M 1997 *Rev. Sci. Instrum.* **68** 2456
     Weingärtner M and Bostanjoglo O 1998 *Surf. Coatings Technol.* **100–101** 85
[80] Spiecker H, Schmidt O, Ziethen Ch, Menke D, Kleineberg U, Ahuja R G, Merkel M, Heinzmann U and
     Schönhense G 1998 *Nucl. Instrum. Methods* A **406** 499
[81] Oelsner A, Schmidt O, Mergel V, Schmidt-Böcking H and Schönhense G 1998 *BESSY Report* p 495
     Oelsner A, Schmidt O, Mergel V, Jagutzki O, Schmidt-Böcking H and Schönhense G, submitted
[82] For PM 3 at BESSY, see Petersen H *et al* 1995 *Rev. Sci. Instrum.* **66** 1
     For I D 12 B at ESRF, see
     Elleaume P 1994 *J. Synchrotron Rad.* **1** 19
[83] Schriever G, Mager S, Naweed A, Engel A, Bergmann K and Lebert R 1998 *Appl. Optics* **37** 1234
     Schriever G *et al* 1998 *J. Appl. Phys.* **83** 4566
[84] Spielmann Ch, Burnett N H, Sartania S, Koppitsch R, Schnürer M, Kan C, Lenzner M, Wobrauschek P and
     Krausz F 1997 *Science* **278** 661
[85] Schütz G, Wagner W, Wilhelm W, Kienle P, Zeller R, Frahm R and Materlik G 1987 *Phys. Rev. Lett.* **58** 737
[86] Schneider C M, Frömter R, Ziethen Ch, Swiech W, Brookes N B, Schönhense G and Kirschner J 1997 *Mater.
     Res. Soc. Symp. Proc.* vol 475 (Pittsburgh, PA: Materials Research Society) p 381
[87] Schneider C M 1997 *J. Magn. Magn. Mater.* **175** 160
[88] Fano U 1969 *Phys. Rev.* **178** 131
     Fano U 1969 *Phys. Rev.* **184** 250
     see also Kessler J *Polarized Electrons* (Berlin: Springer)
[89] Meier F and Zakharchenya B P (eds) 1984 *Optical Orientation* (Amsterdam: North-Holland)
[90] Schneider C M, Holldack K, Kinzler M, Grunze M, Oepen H P, Schäfers F, Petersen H, Meinel K and Kirschner J
     1993 *Appl. Phys. Lett.* **63** 2432
[91] Weinberger P 1990 *Electron Scattering Theory for Ordered and Disordered Matter* (Oxford: Oxford University
     Press)
     Weinberger P *et al* 1993 *Phys. Rev.* B **47** 10154
     Weiberger P 1999 private communication
     Kudrnovsky J *et al* 1997 *Phys. Rev. Lett.* **78** 358
[92] Tonner B P, Harp G R, Koranda S F and Zhang J 1992 *Rev. Sci. Instrum.* **63** 564
[93] Kuch W, Frömter R, Gilles J, Hartmann D, Ziethen Ch, Schneider C M, Schönhense G, Swiech W and
     Kirschner J 1998 *Surf. Rev. Lett.* **5** 1241
[94] Berger A, Linke U and Oepen H P 1992 *Phys. Rev. Lett.* **68** 839
[95] Oepen H P, Berger A, Schneider C M, Reul T and Kirschner J 1993 *J. Magn. Magn. Mater.* **121** 490
[96] Oepen H P and Kirschner J 1989 *Phys. Rev. Lett.* **62** 819
[97] Swiech W, Frömter R, Schneider C M, Kuch W, Ziethen Ch, Schmidt O, Fecher G H, Schönhense G and
     Kirschner J 1998 *Electron Microscopy (Cancun)* p 511

[98] Chikazumi S 1994 *Physics of Magnetism* (Malabor, FL: Wiley–Krieger)
[99] Unguris J, Celotta R J and Pierce D T 1991 *Phys. Rev. Lett.* **67** 140
[100] Unguris J, Celotta R J and Pierce D T 1997 *Phys. Rev. Lett.* **79** 2734
[101] Schneider C M, Meinel K, Kirschner J, Neuber M, Wilde V, Grunze M, Holldak K, Celinski Z and Baudelet F J 1996 *Magn. Magn. Mater.* **162** 7
[102] Rührig M, Schäfer R, Hubert A, Mosler R, Wolf J A, Demokritov S and Grünberg P 1991 *Phys. Status Solidi* a **125** 635
[103] Schneider C M, Frömter R, Ziethen Ch, Swiech W, Brookes N B, Schönhense G and Kirschner J 1997 *ICMFS: Int. Coll. Magnetic Films and Surfaces, (Brisbane)* Conference Digest p 132
Schneider C M, Frömter R, Ziethen Ch, Swiech W, Kuch W, Gilles J, Seider M, Schönhense G and Kirschner J to be published
[104] Freyss M, Stoeffler D and Dreyssé H 1997 *Phys. Rev.* B **56** 6047
[105] Johnson M T, van de Vorst M T H, Bloemen P J H, Coehoorn R, Reinders A, aan de Stegge J and Jungblut R 1995 *Phys. Rev. Lett.* **75** 4686
[106] Kudrnovský J, Drchal V, Coehoorn R, Ŝob M and Weinberger P 1997 *Phys. Rev. Lett.* **78** 358
[107] O'Brien W L and Tonner B P 1994 *Phys. Rev.* B **49** 15 370
[108] Schulz B and Baberschke K 1994 *Phys. Rev.* B **50** 13 467
[109] Reimer L 1985 *Scanning Electron Microscopy* (Berlin: Springer) ch 6.3
[110] Reimer L 1997 *Transmission Electron Microscopy* 4th edn (Berlin: Springer) ch 6.8
[111] Nepijko S A, Sedov N N and Schönhense G *Advances in Imaging and Electron Physics* ed P W Hawkes (in print)
[112] Marx G K L, Dunin v. Przychowski M, Schönhense G and Schneider C M, submitted
[113] Marx G K L, Elmers H J and Schönhense G submitted
[114] Oppneer P M T M, Stichte J and Kübler J 1992 *Phys. Rev.* B **45** 10 924
[115] Erskine J L *et al* 1973 *Phys. Rev.* B **8** 1239
[116] Maran G D 1970 *Phys. Rev.* B **2** 4334
[117] Sass J K 1975 *Surf. Sci.* **51** 199–212
[118] Cherepkov N A 1996 Photoionization of polarized atoms: applications to free atoms and ferromagnets *Selected Topics in Electron Physics* ed H Kleinpoppen and M C Campbell (New York: Plenum) p 385
[119] Roth Ch, Rose H B, Hillebrecht F U and Kisker E 1993 *Solid State Commun.* **86** 647
[120] Hillebrecht F U, Kinoshita T, Spanke D, Dresselhaus J, Roth Ch, Rose H B and Kisker E 1995 *Phys. Rev. Lett.* **75** 2224
[121] Rampe A, Güntherodt G, Hartmann D, Menk J, Scheunemann T and Feder R 1998 *Phys. Rev.* B **57** 14 370
[122] Bansmann J, Getzlaff M, Ostertag Ch and Schönhense G 1996 *Surf. Sci.* **352–64** 898
Getzlaff M, Ostertag Ch, Fecher G H, Cherepkov N A and Schönhense G 1994 *Phys. Rev. Lett.* **73** 3030–3
[123] Henk J and Feder R 1997 private communication
[124] Henk J, Halilov S V, Scheunemann T and Feder R 1994 *Phys. Rev.* B **50** 8130
[125] Scheunemann T, Halilov S V, Henk J and Feder R 1994 *Solid State Commun.* **91** 487
[126] Dove D B 1963 *J. Appl. Phys.* **34** 2067
[127] Katayama T N N, Okusawa N, Miyauchi Y, Koide T, Shidara T, Suzuki Y and Yusas S 1998 *J. Magn. Magn. Mater.* **177–181** 1251–2
[128] Bauer E 1998 *Surf. Rev. Lett.* **5** 1275
[129] Haider M, Uhlemann S, Schwan E, Rose H, Kabius B and Urban K 1998 *Nature* **392** 768
[130] Haider M, Rose H, Uhlemann S, Schwan E, Kabius B and Urban K 1998 *Ultramicroscopy* **75** 53
[131] Rose H 1999 *Ultramicroscopy* **78** 13